NASA
Technical
Paper
2982

April 1990

Low-Speed Wind-Tunnel Investigation of the Flight Dynamic Characteristics of an Advanced Turboprop Business/Commuter Aircraft Configuration

Paul L. Coe, Jr.,
Steven G. Turner,
and D. Bruce Owens

NASA

NASA Technical Paper 2982

1990

Low-Speed Wind-Tunnel Investigation of the Flight Dynamic Characteristics of an Advanced Turboprop Business/Commuter Aircraft Configuration

Paul L. Coe, Jr.,
Steven G. Turner,
and D. Bruce Owens
Langley Research Center
Hampton, Virginia

National Aeronautics and Space Administration
Office of Management
Scientific and Technical Information Division

Summary

An investigation was conducted to determine the low-speed flight dynamic behavior of a representative, advanced turboprop business/commuter aircraft concept. The investigation was conducted using model free-flight tests in the Langley 30- by 60-Foot Tunnel. In support of the free-flight tests, conventional static, dynamic, and free-to-roll oscillation tests were performed.

The model free-flight test pilots commented that for angles of attack below the stall, the baseline configuration was stable and easy to fly. The pilots found that the basic airframe had satisfactory damping about all three axes and was responsive to longitudinal and lateral-directional control inputs. At the stall angle of attack the free-flight tests of the baseline configuration were terminated because of an abrupt wing drop and autorotative departure against full corrective roll control. Conventional wind-tunnel tests showed that the wing drop was due to an abrupt asymmetric wing stall that produced a pronounced rolling moment.

Additional free-flight tests of the configuration, modified to include wing leading-edge devices, were conducted. These modifications consisted of outboard-wing leading-edge droops and outboard Krüger flaps. Tests of the modified configuration showed a significant improvement in roll control and a substantial increase in roll damping. Even at poststall angles of attack (i.e., an angle of attack α on the order of 20°), the pilots indicated that the overall flying qualities were acceptable and no significant stability or control problems were evident for either the longitudinal or lateral-directional axes. Free-flight tests of the configuration with the modified leading edges were terminated at $\alpha = 24°$ to 27° because of a loss of pitch control. Static force tests showed a consistent reduction in elevator effectiveness for an angle of attack of 24°.

Model free-flight tests conducted to explore engine-out trim and flight dynamics were limited to the model configuration employing outboard-wing leading-edge droops at an assumed approach angle of attack of approximately 12°. Free-flight tests showed that the model could not achieve yaw trim while holding the angle of sideslip β at 0°; also, engine-out yaw trim could only be achieved for sideslipped conditions with $\beta \approx 10°$ and with the rudder fully deflected to 25°. In this trim condition the rudder was fully deflected and there was insufficient rudder available for directional control. The pilot noted that although he could achieve engine-out roll trim, the intermittent or unsteady nature of the wing stall on the side of the inoperative engine resulted in an abrupt roll-off tendency that required an excessive pilot work load to control.

Introduction

Previous studies have identified potentially significant improvements in transport-aircraft fuel economy that may result through the incorporation of advanced turboprop propulsion systems. (See ref. 1.) In addition, experimental studies have indicated that both wing- and aft-fuselage-mounted advanced turboprop transport configurations are feasible. (See, for example, ref. 2.) The potential success of the application of advanced turboprop concepts to transport-category aircraft configurations has resulted in an interest in the application of advanced turboprop concepts to business/commuter aircraft.

A cooperative NASA/industry research effort has been initiated to explore the low-speed performance, static and dynamic stability and control, and flying qualities characteristics of a representative twin-engine business/commuter aircraft concept. The configuration incorporates single-rotation pusher propellers that are pylon-mounted on the aft fuselage. Reference 3 presents results of initial static wind-tunnel tests of this representative aircraft concept. The test data show that the configuration exhibits satisfactory low-speed performance and stability and control characteristics for angles of attack α below the stall. However, the wind-tunnel results indicate that the configuration exhibits undesirable characteristics in the stall/poststall α range. Specifically, the configuration exhibits an abrupt asymmetric wing stall with correspondingly large rolling and yawing moments and a simultaneous reduction in aileron effectiveness. The propeller inflow apparently improves the flow conditions over the inboard portions of the wing and pylons and thereby provides increased lift at poststall angles of attack. For conditions with one engine out, the asymmetric loss of this increased lift results in very large engine-out rolling moments in the stall/poststall α range. Furthermore, although the engine-out yawing moment is principally due to the thrust-related moment of the operating engine, a reduction in vertical-tail/rudder effectiveness resulted in marginal engine-out yaw trim.

The investigation reported in reference 3 was limited to static tests and did not provide any information relating to the dynamic behavior of the configuration. Previous experience with aircraft exhibiting stall characteristics similar to those of the present configuration has shown the damping in roll to be seriously degraded at the stall. Thus, if the present baseline configuration were to inadvertently exceed the stall angle of attack, the combination of asymmetric wing stall, reduced aileron effectiveness, and

degraded roll damping would possibly result in a sharp roll-off followed by an autorotation and departure from controlled flight.

The present investigation was conducted to determine the low-speed, poststall flight dynamic behavior of the advanced turboprop business/commuter aircraft configuration. The investigation consisted of both conventional static and dynamic force and moment tests and wind-tunnel model free-flight tests.

Symbols

All longitudinal forces and moments are referred to the wind-axis system, and all lateral-directional forces and moments are referred to the body-axis system. (See fig. 1.) The aircraft aerodynamic moments are referred to a moment reference center located longitudinally at 18.36 percent of the wing mean aerodynamic chord. (See fig. 2(a).)

b	wingspan, ft
C_D	drag coefficient, Drag/$q_\infty S$
C_L	lift coefficient, Lift/$q_\infty S$
C_l	rolling-moment coefficient, Rolling moment/$q_\infty Sb$
ΔC_l	incremental rolling-moment coefficient
C_m	pitching-moment coefficient, Pitching moment/$q_\infty S\bar{c}$
C_n	yawing-moment coefficient, Yawing moment/$q_\infty Sb$
ΔC_n	incremental yawing-moment coefficient
C_Y	side-force coefficient, Side force/$q_\infty S$
ΔC_Y	incremental side-force coefficient
c	local wing chord, ft
$\bar{c}$	mean aerodynamic chord, ft
D	propeller diameter, ft
g	acceleration due to gravity ($1g \approx 32.174$ ft/sec^2)
I_X, I_Y, I_Z	moment of inertia about X-, Y-, or Z-axis, respectively
i_t	horizontal tail incidence angle, positive with trailing edge down, deg
J	propeller advance ratio, V_∞/ND
K_p	roll-rate feedback gain, deg δ_a/deg/sec of p
K_q	pitch-rate feedback gain, deg δ_e/deg/sec of q
K_r	yaw-rate feedback gain, deg δ_r/deg/sec of r
K_α	angle-of-attack feedback gain, deg δ_e/deg α
k	reduced-frequency parameter, $\omega b/2V_\infty$
L_α	lift per unit angle of attack per unit momentum, $(q_\infty S/mV_\infty)C_{L_\alpha}$, per second
m	aircraft mass, slugs
N	propeller rotational speed, rps
n/α	steady-state normal acceleration change per unit change in angle of attack for an incremental horizontal tail deflection at constant airspeed, g units/rad
p	roll rate, rad/sec
q	pitch rate, rad/sec
q_∞	free-stream dynamic pressure, lb/ft^2
$R_{\bar{c}}$	Reynolds number based on $\bar{c}$
r	yaw rate, rad/sec
S	wing reference area, ft^2
T_c'	= Model thrust/$q_\infty S$
T_R	roll-mode time constant, $t_{1/2}/0.693$
t	time, sec
t_2	time to double amplitude, sec
$t_{1/2}$	time to half-amplitude, sec
V_∞	free-stream velocity, ft/sec
WS	wing station, in.
X, Y, Z	body-axis system (see fig. 1)
y	semispan location, ft
α	angle of attack, deg
β	angle of sideslip, deg
$\dot{\beta}$	rate of change of sideslip, rad/sec
δ_a	aileron deflection, $(\delta_{a,R} + \delta_{a,L})/2$

δ_e	elevator deflection, positive with trailing edge down, deg
δ_f	wing trailing-edge flap deflection, positive with trailing edge down, deg
δ_r	rudder deflection, positive with trailing edge left, deg
ζ_{DR}	Dutch roll damping ratio
ζ_{sp}	longitudinal short-period mode damping ratio
ϕ	roll angle about X body axis, deg
$\dot{\phi}$	rolling velocity about X body axis, $\frac{\partial\phi}{\partial\left(\frac{2V_\infty t}{b}\right)}$, deg
$\dot{\phi}_o$	$= \dot{\phi}\|_{t=0}$
ω	angular velocity, rad/sec
ω_{DR}	Dutch roll undamped natural frequency, rad/sec
ω_{sp}	longitudinal, short-period undamped natural frequency, rad/sec

Subscripts:

L	left
R	right

Stability derivatives:

$$C_{l_\beta} = \frac{\partial C_l}{\partial \beta} \qquad C_{n_\beta} = \frac{\partial C_n}{\partial \beta} \qquad C_{Y_\beta} = \frac{\partial C_Y}{\partial \beta}$$

$$C_{l_{\dot{\beta}}} = \frac{\partial C_l}{\partial \frac{\dot{\beta}b}{2V_\infty}} \qquad C_{n_{\dot{\beta}}} = \frac{\partial C_n}{\partial \frac{\dot{\beta}b}{2V_\infty}} \qquad C_{l_{\delta_a}} = \frac{\partial C_l}{\partial \delta_a}$$

$$C_{n_{\delta_a}} = \frac{\partial C_n}{\partial \delta_a} \qquad C_{Y_{\delta_a}} = \frac{\partial C_Y}{\partial \delta_a} \qquad C_{m_{\delta_e}} = \frac{\partial C_m}{\partial \delta_e}$$

$$C_{l_{\delta_r}} = \frac{\partial C_l}{\partial \delta_r} \qquad C_{n_{\delta_r}} = \frac{\partial C_n}{\partial \delta_r} \qquad C_{Y_{\delta_r}} = \frac{\partial C_Y}{\partial \delta_r}$$

$$C_{l_p} = \frac{\partial C_l}{\partial \frac{pb}{2V_\infty}} \qquad C_{n_p} = \frac{\partial C_n}{\partial \frac{pb}{2V_\infty}} \qquad C_{l_r} = \frac{\partial C_l}{\partial \frac{rb}{2V_\infty}}$$

$$C_{n_r} = \frac{\partial C_n}{\partial \frac{rb}{2V_\infty}} \qquad C_{L_\alpha} = \frac{\partial C_L}{\partial \alpha}$$

Model and Tests

Model Description

The geometric characteristics of the baseline configuration and subsequent configuration modifications are depicted in figure 2. The model was constructed such that the mass and geometric properties were scaled to simulate a representative business/commuter aircraft for the purpose of determining flight characteristics from free-flight tests in the Langley 30- by 60-Foot Tunnel. Geometric and mass characteristics of the model are shown in table I. Because the intent of the investigation was to explore the high-lift landing-approach condition, the wing had the trailing-edge flaps deflected 35°. Model control surface deflections were $\delta_a = 20°$ to $-20°$, $\delta_e = 15°$ to $-25°$, and $\delta_r = 20°$ to $-20°$. Horizontal tail incidence angle i_t could be varied from 2° to $-10°$ in order to provide an extended range of pitch trim.

The model was powered with two 5-bladed propeller systems that were driven by air turbines located internal to the nacelles. (See figs. 2(c) and 2(d).) Propeller advance ratios J of 0.52 and 0.45 were selected to provide model thrust coefficients T_c' of 0.1 and 0.2 per engine, respectively.

Test

The free-flight test technique is illustrated in figure 3(a) and described in reference 4. In such tests powered, instrumented dynamically scaled models are flown by remote control in level flight up to stall/departure to investigate stability and control characteristics and to identify any tendencies of the configuration to depart from controlled flight. The free-flight control system incorporates high-performance electropneumatic actuators, rate gyros, accelerometers, α and β sensors, and also a minicomputer to simulate the flight control system for a given configuration. This system permits a rapid evaluation of various control laws and/or an evaluation of a range of levels of artificial stabilization and control system gains. In each axis, pilot stick and trim inputs may be combined with the stability augmentation system (SAS) signals. The SAS is comprised of angular-rate feedbacks about each of the three body axes. The rate damper signals used in the control laws are provided by a three-axis gyro package and can be independently switched on or off about each axis. A diagram of the control laws used for the present investigation is presented in figure 3(b). Typical free-flight test results are in the form of pilot comments, movies, and time histories of flight motions. A photograph showing the model during free-flight tests is presented in figure 3(c).

Static force tests were conducted in the Langley 30- by 60-Foot and 12-Foot Low-Speed Tunnels at nominal values of $q_\infty = 6$ psf and 3 psf, respectively. These values of dynamic pressure corresponded to values of $R_{\bar{c}}$ of 0.50×10^6 and 0.38×10^6. For static tests the angle of attack ranged from $-8°$ to 28° with

sideslip angles of ±5°. A photograph showing the model mounted for static tests in the Langley 30- by 60-Foot Tunnel is presented in figure 3(d).

Dynamic forced-oscillation tests were made about the roll and yaw axes in the Langley 30- by 60-Foot Tunnel. The forced-oscillation test technique is described in reference 5. For forced-oscillation tests the angle of attack ranged from −10° to 40°. Sketches showing the model mounted for forced-oscillation tests in roll and yaw are presented as figures 3(e) and 3(f), respectively. Corresponding photographs showing the model mounted for forced-oscillation tests in roll and yaw are presented as figures 3(g) and 3(h), respectively. Data were obtained at an oscillation reduced-frequency parameter k of 0.4 over an angular amplitude of ±5°.

Free-to-roll tests were conducted with the model in the Langley 12-Foot Low-Speed Tunnel. In the free-to-roll tests the model was mounted on an apparatus consisting of two concentric barrels attached by ball bearing assemblies that allowed the model to rotate freely about its roll axis. More information about the free-to-roll test technique may be found in reference 6.

Results and Discussion

The results and discussion are presented in accordance with the following outline:

Figure

Longitudinal aerodynamic characteristics:
- Reynolds number effects and comparison with previous data 4
- Effect of power on longitudinal aerodynamic characteristics 5
- Effect of power on elevator effectiveness 6
- Effect of wing leading-edge devices 7–9

Lateral-directional aerodynamic characteristics:
- Effect of power on lateral-directional stability and rudder effectiveness 10, 11
- Effect of power on aileron effectiveness 12
- Effect of power on lateral-directional characteristics 13
- Effect of power on roll and yaw damping 14, 15
- Effect of wing leading-edge devices 16–20

Engine-out aerodynamic characteristics:
- Engine-out forces and moments 21, 22
- Engine-out trim characteristics 23–26

Evaluation of flying qualities:
- Predicted longitudinal flying qualities 27
- Evaluation of longitudinal flying qualities
- Predicted lateral-directional flying qualities 28 30
- Evaluation of lateral-directional flying qualities
- Evaluation of engine-out roll and yaw trim

Longitudinal Aerodynamic Characteristics

Reynolds number effects and comparison with previous data. Figure 4 presents static longitudinal data from the present tests for the complete baseline configuration with $\delta_f = 35°$. These data were obtained for a test Reynolds number of 0.5×10^6. Also presented in figure 4 are data from reference 3 (recomputed for a moment reference center consistent with that of the present tests, i.e., $0.1836\bar{c}$) for values of test Reynolds numbers of 0.55×10^6 and 1.75×10^6. It should be noted that for comparable values of $R_{\bar{c}}$, the data of the present tests are in good agreement with those of reference 3.

The data of figure 4 show a marked sensitivity of $R_{\bar{c}}$. Although not presented herein, additional data presented in reference 3 show that Reynolds number effects are insignificant for $R_{\bar{c}} > 1.75 \times 10^6$, and therefore the aerodynamic characteristics presented for $R_{\bar{c}} = 1.75 \times 10^6$ are representative of those for an assumed full-scale aircraft flight condition corresponding to a value of $R_{\bar{c}}$ on the order of 5×10^6. It should be noted that although the data of figure 4 show a marked sensitivity to $R_{\bar{c}}$, the fundamental nature of the data is independent of $R_{\bar{c}}$. For example, data measured for both $R_{\bar{c}} = 0.5 \times 10^6$ and $R_{\bar{c}} = 1.75 \times 10^6$ show that at the onset of stall, there is an initial stable break in C_m followed by an abrupt stall (indicative of complete separation) and subsequent pitch-up. Subsequent figures will show comparisons (when available) of data from the present tests for $R_{\bar{c}} = 0.5 \times 10^6$ with data from reference 3 for $R_{\bar{c}} = 1.75 \times 10^6$. (Note that the data of ref. 3 are recomputed for a moment reference center consistent with the present tests.) In each case, such comparisons show that the fundamental nature of the data is independent of $R_{\bar{c}}$.

Model free-flight tests are conducted at relatively low speeds and, consequently, at relatively low values of $R_{\bar{c}}$. For the present investigation, the $R_{\bar{c}}$ of the model free-flight tests is on the order of 0.5×10^6. Previous experience with the model free-flight technique in the 30- by 60-Foot Tunnel and correlation of such tests have shown that although Reynolds number sensitive configurations may exhibit stall at premature angles of attack, the stall/poststall flight

dynamic behavior is accurately portrayed. This result is further substantiated by the consistency of the present data (measured for values of $R_{\bar{c}}$ corresponding to those of the model free-flight tests, i.e., $R_{\bar{c}} \approx 0.5 \times 10^6$) with the data presented in reference 3 (measured for significantly higher values of $R_{\bar{c}}$).

Effect of power on longitudinal aerodynamic characteristics. The data of figure 5 show that the configuration experiences an abrupt stall followed by a pitch-up. The data further show that power does not influence the angle of attack at which stall occurs, and that prior to stall, power effects are limited to the vector components and the line of action of the thrust force. For poststall angles of attack, power produces a significant increase in lift and a nose-down increment in pitching moment. Visual observation of wool surface tufts showed that the poststall power effects were attributable to the propeller inflow providing improved flow conditions on that portion of the inboard wing ahead of the propeller disk, as well as on the nacelle and pylon surfaces.

Effect of power on elevator effectiveness. Elevator effectiveness is summarized in figure 6. As can be seen for the unpowered condition, elevator effectiveness is markedly reduced in the poststall angle-of-attack range. This result is typical of "T"-tail designs at poststall angles of attack because the elevator operates in the stalled wake of the wing. The increase in elevator effectiveness (due to power) in the poststall α range is directly related to the previously mentioned improvement in the poststall flow conditions on the inner wing, and also to subsequent improvement in the empennage flow field.

Effect of wing leading-edge devices. Subsequent discussions of the lateral-directional aerodynamic characteristics will show that the configuration exhibits a pronounced rolling moment at the stall angle of attack and $\beta = 0°$. This phenomenon is typically found to be characteristic of configurations with an abrupt stall pattern. The lateral-directional aerodynamic data will further show that at the stall, the configuration experiences a marked reduction in both aileron effectiveness and roll damping. The combination of large rolling moments, loss of aileron effectiveness, and reduced roll damping typically results in the stall being followed by a sharp roll-off and subsequent uncontrolled autorotation and departure from controlled flight.

In view of the preceding discussion, an outboard-wing leading-edge droop was designed to delay separation on the outer portion of the wing and thereby reduce the severity of the asymmetric stall and provide reduced poststall rolling moments, improved aileron effectiveness, and increased roll damping. In order to provide a figure of merit, two additional leading-edge devices were designed and tested, and these correspond to (1) a full-span Krüger flap, and (2) an outboard Krüger flap. (See figs. 2(e) and 2(f), respectively.)

Figures 7, 8, and 9 show the effects of the various wing leading-edge devices on the static longitudinal aerodynamic characteristics of the configuration. As might be expected, the full-span Krüger flap provides the most effective form of leading-edge treatment for the poststall α range. However, significant improvements in the static poststall longitudinal aerodynamic characteristics are provided with the outboard droop; furthermore, the effectiveness of the outboard droop is comparable to that of the outboard Krüger flap. It should be noted that the obvious advantage of such an outboard-wing leading-edge droop is that it is designed for minimal effect on cruise performance (see, for example, refs. 7–11) and, unlike the Krüger flap systems, would not require complex mechanisms to stow the device for cruise conditions. Figures 7 and 8 show that the wing leading-edge devices provided an improvement in the poststall lift characteristics of both the unpowered and powered ($T_c' = 0.2$) configurations, and that this improvement is achieved with only minimal influence on pitching moment.

Figure 9 shows the effect of both wing leading-edge devices and power on elevator effectiveness. As can be seen, outboard-wing leading-edge devices provide only relatively small improvements in poststall elevator effectiveness. However, as noted in the discussion of figure 6, power is seen to provide significant improvements in elevator effectiveness for poststall angles of attack. Since the outboard-wing leading-edge devices improve the stall characteristics on the outer portion of the wing (whereas power improves the stall characteristics on the inner portion of the wing), the results presented in figure 9 are as anticipated.

Lateral-Directional Aerodynamic Characteristics

Effect of power on lateral-directional stability and rudder effectiveness. Figures 10 and 11, respectively, present the effect of thrust on static lateral-directional stability and on rudder effectiveness of the complete baseline configuration. The data show that for the unpowered condition, the configuration experiences low values of positive effective dihedral ($-C_{l_\beta}$). The data further show that for

the unpowered condition, there is a marked reduction in directional stability and rudder effectiveness for poststall angles of attack. The reduction in directional stability and rudder effectiveness is similar to that previously discussed for the elevator effectiveness and results from the vertical tail and rudder being immersed in the stalled wake of the wing. As noted with regard to elevator effectiveness, power improves the wake flow field over the empennage surfaces for poststall conditions. This improvement in the wake flow field results in improved directional stability and rudder effectiveness as well as improved elevator effectiveness. It should be noted that power also results in a significant increase in positive effective dihedral ($-C_{l_\beta}$). This increase in effective dihedral is related to the previously discussed improved flow conditions on the inner wing and, consequently, an improvement in the spanwise load distribution.

Effect of power on aileron effectiveness. Figure 12 presents the effect of thrust on aileron effectiveness for the complete baseline configuration. As can be seen for poststall angles of attack, aileron effectiveness is markedly reduced. The reduction in poststall aileron effectiveness is a result of flow separation on the outboard portion of the wing. Power is found to primarily influence the flow on the inboard portion of the wing, and therefore it has only a small influence on aileron effectiveness. (See fig. 12.)

Effect of power on lateral-directional characteristics. Figure 13 presents the variation of the lateral-directional force and moment coefficients with angle of attack at $\beta = 0°$. At the stall angle of attack a pronounced rolling moment (in addition to a smaller yawing moment), which is unaffected by symmetric power, is observed. This phenomenon is considered a result of an asymmetric wing stall and is found to be a characteristic of wings having an abrupt stall pattern. Depending on roll damping, the combination of large rolling moments and loss of aileron effectiveness at the stall may result in a sharp roll-off followed by an autorotation and departure from controlled flight.

Effect of power on roll and yaw damping. Damping characteristics obtained from dynamic forced-oscillation tests about the roll and yaw axes are presented in figures 14 and 15, respectively. The data of figure 14 show that at the stall, the roll damping is markedly degraded. This phenomenon is a direct result of the previously mentioned flow separation on the outboard portion of the wing. For conditions with $T'_c = 0.2$, the roll damping is seen to remain slightly stable at the stall, whereas for conditions with the propellers windmilling, the roll damping becomes unstable. This favorable effect of power on roll damping is undoubtedly associated with the propeller flow-field interactions on the inboard wing panels and engine pylons.

Figure 15 shows that the configuration is well damped in yaw and that thrust extends the range of angle of attack for which the yaw damping remains stable from $-10°$ to a range of $-10°$ to $40°$.

Effect of wing leading-edge devices. The preceding results show that at the stall, the baseline configuration experiences a pronounced rolling moment at $\beta = 0°$ and a marked reduction in both aileron effectiveness and roll damping. As noted previously, an outboard-wing leading-edge droop (see figs. 2(e) and 2(f)) was designed in an attempt to improve the flow on the outer portion of the wing and thereby improve the aforementioned lateral-directional deficiencies. To provide a figure of merit, additional leading-edge devices were designed and tested—a full-span Krüger flap and an outboard Krüger flap. (See figs. 2(e) and 2(f), respectively.) Figures 16 through 20 show the effects of these various wing leading-edge devices on the lateral-directional aerodynamic characteristics.

Figure 16 and 17 present the effect of wing leading-edge devices on the static lateral-directional stability and rudder effectiveness, respectively, of the complete configuration. The data show that the outboard-wing leading-edge devices provide only a relatively small improvement compared to power which provides a significant improvement in poststall directional stability and rudder effectiveness. The phenomenon of reduced poststall directional stability and rudder effectiveness has been discussed previously and is attributed to the vertical tail and rudder operating in the stalled wake of the wing. Since outboard-wing leading-edge devices improve the stall characteristics on the outer portion of the wing and power improves the stall characteristics on the inner portion of the wing, the effects of wing leading-edge devices and power on poststall directional stability and rudder effectiveness are as anticipated.

Figure 18 presents the effect of wing leading-edge devices on aileron effectiveness. As can be seen, all the wing leading-edge devices were effective in providing improved poststall aileron effectiveness. It is, however, noteworthy that the outboard droop provided results comparable to those of both the full- and part-span Krüger flaps. This result is, of course, associated with the improvements in flow conditions

over the outboard portion of the wing and, consequently, the improvement in flow conditions over the ailerons. As previously noted, power has little influence on aileron effectiveness.

The effect of wing leading-edge devices on lateral-directional characteristics at $\beta = 0°$ is presented in figure 19. As previously noted, the large rolling moment for the configuration with the clean leading edge is a result of asymmetric wing stall and is a characteristic of configurations with an abrupt stall pattern. Therefore, leading-edge concepts that reduce the abrupt nature of the wing stall (see figs. 7 and 8) would, as demonstrated in figure 19, be expected to reduce the magnitude of the rolling moment.

Figure 20 presents the effect of wing leading-edge devices on roll damping. The results presented were obtained using the free-to-roll technique described in reference 6. An estimate of the relative roll-damping characteristics for the modified wing leading-edge configurations may be obtained using the approximation to the rolling-mode equation (ref. 12). Solution of the approximate rolling-mode equation yields an expression for the rolling velocity $\dot{\phi}$:

$$\dot{\phi} = \dot{\phi}_o e^{\frac{\rho S b^3}{8 I_X} \frac{2V_\infty}{b} C_{l_p} t} \tag{1}$$

A comparison of the times required to achieve approximately equal roll rates for the baseline and modified wing leading-edge configurations yields

$$C_{l_{p,\text{modified}}} = C_{l_{p,\text{baseline}}} \times \frac{t_{\text{baseline}}}{t_{\text{modified}}} \tag{2}$$

Values of roll damping for the baseline configuration have been obtained using the forced-oscillation technique and are presented in figure 14. Therefore, using the data of figure 14 and observed values of the time required to achieve approximately equal roll rates for the baseline and modified leading-edge configurations (eq. (2)) yields estimates for the roll damping of the configurations with the modified leading edges. The results indicated that all wing leading-edge devices tested produced about the same level of improvement in roll damping. Because of the uncertainties in the measurements, the results are presented as a cross-hatched band and are compared with the forced-oscillation result for the baseline configuration in figure 20.

Engine-Out Aerodynamic Characteristics

Engine-out forces and moments. Figures 21 and 22 present the incremental rolling-moment, yawing-moment, and side-force coefficients for conditions with the left-engine inoperative. Figure 21 presents the results for the baseline configuration with the clean leading edge, and figure 22 presents corresponding results for the configuration with the various leading-edge devices tested. A consideration of the data shows that the various leading-edge devices had essentially no effect on the engine-out force and moment coefficients.

An analysis of the data of figures 21 and 22 shows that the engine-out yawing moment is approximately the product of the thrust vector of the operative engine and the lateral displacement of that engine from the configuration centerline. The data of figures 21 and 22 also show that large engine-out rolling moments are produced in the direction of the inoperative engine. As noted previously, flow visualization has indicated that for poststall angles of attack, the propeller slipstream provides improved flow conditions over the inboard portion of the wing and pylon. Thus, the engine-out rolling moments are attributed to the loss of the favorable flow interaction and, consequently, loss of lift on the inboard wing and pylon on the side of the inoperative engine.

Engine-out trim characteristics. An analysis of the data of figures 21 and 22 shows that the engine-out yawing moment is approximately the product of the thrust vector of the operative engine and the lateral displacement of that engine from the moment reference center. Therefore, the engine-out yawing moment can be expressed as

$$\Delta C_n = \frac{y}{b} T'_{c,\text{oe}} \tag{3}$$

where it is, of course, recognized that for steady-state trim conditions,

$$T'_{c,\text{oe}} = C_D \tag{4}$$

where the subscript oe denotes the operative engine and y denotes the semispan location. Therefore, based on linear theory, ΔC_n required to trim can be represented as

$$\Delta C_n = \frac{y}{b} C_D = C_{n_\beta}\beta + C_{n_{\delta_r}}\delta_r + C_{n_{\delta_a}}\delta_a \tag{5}$$

Noting that $C_{n_{\delta_a}}$ is negligible (see figs. 12 and 18), the rudder deflection required for trim may be obtained from equation (5) and is given by the relationship

$$\delta_r = \frac{\frac{y}{b} C_D - C_{n_\beta}\beta}{C_{n_{\delta_r}}} \tag{6}$$

Figures 23 and 24 present the variation of rudder deflection versus α required for left-engine-out yaw

trim. The calculations are based on data from reference 3 ($R_{\bar{c}} = 2.0 \times 10^6$) and from the present test data ($R_{\bar{c}} = 0.5 \times 10^6$). If the maximum value of rudder deflection δ_r is increased from $\pm 20°$ to $\pm 25°$, the data show that for angles of attack at and below the stall, engine-out yaw trim can be achieved with sideslip angles on the order of only $\beta = 5°$. However, for angles of attack above the stall, the data show that even for $\delta_r = \pm 25°$, engine-out yaw trim can be achieved only with large values of sideslip. For example, consider the data of figure 23(a) which were measured at $R_{\bar{c}} = 2.0 \times 10^6$. For $\alpha = 15°$ and the rudder fully against the engine-out yawing moment ($\delta_r = -25°$), a sideslip angle of approximately 15° is required for yaw trim with the left engine out. Such values of sideslip may be impractical, and furthermore they are probably outside the range for which the linear theory of the present analysis is valid. The large value of sideslip required to achieve engine-out yaw trim for poststall angles of attack is due to the abrupt nature of the stall resulting in high drag and, hence, a high level of thrust-related yawing moment required to be trimmed.

The preceding analysis is based on linear theory, and the results presented are based on values of directional stability obtained over a limited sideslip range (i.e., $\beta = \pm 5°$); however, data obtained from engine-out flight tests, which will be discussed subsequently, agree quite well with the results presented in figure 24.

The rolling moment required for engine-out roll trim can be represented, based on linear theory, by the expression

$$\Delta C_l = C_{l_\beta}\beta + C_{l_{\delta_a}}\delta_a + C_{l_{\delta_r}}\delta_r \tag{7}$$

Substituting equation (6) for δ_r into equation (7) yields

$$\Delta C_l = \left(C_{l_\beta} - \frac{C_{l_{\delta_r}} C_{n_\beta}}{C_{n_{\delta_r}}}\right)\beta + \left(\frac{C_{l_{\delta_r}}}{C_{n_{\delta_r}}}\frac{y}{b}C_D\right) + C_{l_{\delta_a}}\delta_a \tag{8}$$

Upon substituting numerical values into equation (8) it is found that the term $C_{l_{\delta_r}}\left(C_{n_\beta}/C_{n_{\delta_r}}\right)$ is small in comparison with C_{l_β} and, thus, equation (8) can be simplified. Solving the simplified equation for δ_a yields

$$\delta_a = \left(\Delta C_l - C_{l_\beta}\beta - \frac{C_{l_{\delta_r}}}{C_{n_{\delta_r}}}\frac{y}{b}C_D\right)\frac{1}{C_{l_{\delta_a}}} \tag{9}$$

Figures 25 and 26 present the variation of δ_a required to provide roll trim for the left-engine-out condition. The calculations are based on the data from reference 3 for $R_{\bar{c}} = 2.0 \times 10^6$ and on the present test data for $R_{\bar{c}} = 0.5 \times 10^6$. It should be noted that the preceding analysis was not intended to consider the incremental rolling moments resulting from asymmetric wing stall, but rather it was intended to consider only the incremental rolling moment associated with engine-out conditions.

The results of the preceding analysis indicate that for the lower angles of attack (i.e., those values of α for which engine-out yaw trim can be achieved), engine-out roll trim can also be achieved through a combination of relatively small values of aileron deflection and sideslip. Furthermore, even for poststall angles of attack, engine-out roll trim can be easily achieved. The improvement in poststall aileron effectiveness afforded by the outboard-wing leading-edge droops (see fig. 18) results in reduced values of aileron deflection necessary for left-engine-out roll trim (see fig. 26).

Evaluation of Flying Qualities

Predicted longitudinal flying qualities. Figure 27 presents two widely used longitudinal flying qualities criteria. Estimated values of $\omega_{sp}, n/\alpha$, L_α/ω_{sp}, and ζ_{sp} are presented for an assumed full-scale business/commuter aircraft operating at several lift coefficients. These estimated values are based on the following: (1) the static aerodynamic data of present test configurations, (2) the estimated values of pitch damping based on the configuration tail geometry, and (3) the full-scale mass and inertias obtained using model free-flight values and the dynamic scaling relationships presented in reference 4. (It is assumed that the present model scale is 0.175.) These estimated values are assumed for lift coefficients C_L of 0.5, 1.0, and 2.0. The highest value of C_L considered (i.e., $C_L = 2.0$) was selected assuming a linear variation of C_L versus α.

Figure 27(a) shows the short-period frequency requirement of reference 13, and figure 27(b) shows the Shomber-Gertsen longitudinal flying qualities criterion of reference 14. As can be seen (based on the criteria of refs. 13 and 14), the assumed, full-scale advanced turboprop business/commuter concept with symmetric power is expected to exhibit satisfactory longitudinal flying qualities.

Evaluation of longitudinal flying qualities. Model free-flight tests were conducted in the Langley 30- by 60-Foot Tunnel (see fig. 3(a)) to evaluate longitudinal and lateral-directional flying qualities (for $1g$ level flight) up to stall-departure. Typically during such tests, representative aircraft control systems are also modeled via a flight control computer. As

noted previously, this system permits rapid evaluation of various control laws and/or evaluation of a range of levels of artificial stabilization and control system gains. For the present investigation, artificial stability was available for the longitudinal axis in the form of angle-of-attack and pitch-rate feedback. Artificial stability, in the form of sideslip and roll- and yaw-rate feedback, was also available for the lateral-directional axis. (See fig. 3(b).)

During the present investigation the longitudinal pilots evaluated various levels of artificial stability; however, they found that the basic airframe had satisfactory damping in pitch and was responsive to longitudinal control input. The longitudinal pilots commented that for angles of attack below the stall, the baseline configuration was easy to fly. The pilots stated that the basic configuration exhibited satisfactory longitudinal flying qualities and did not require any form of artificial stability. This result is in good agreement with the predicted results based on the flying qualities criteria presented in figure 27.

Free-flight tests of the baseline configuration were limited to angles of attack below the stall. At the stall angle of attack the free-flight tests of the baseline configuration were terminated because of an abrupt wing drop and autorotative departure which the lateral-directional pilot was unable to control. This phenomenon will be discussed in a subsequent section relating to the lateral-directional flying qualities.

Free-flight tests were also conducted for the configuration incorporating the outboard-wing leading-edge droop and the outboard Krüger flap. (See figs. 2(e) and 2(f).) In these studies wool tufts were attached to the wing to provide an assessment of wing-surface flow conditions. Free-flight tests of the configuration with either the outboard-wing leading-edge droop or the outboard Krüger flap showed similar results. Specifically, free-flight tests of the configuration with either of the modified outboard leading edges showed that for $\alpha \approx 10°$, the model flew quite well and the flow over the wing surface was well attached. Upon increasing the angle of attack to approximately 16°, wool surface tufts showed evidence of intermittent stall over the inboard portion of the wing. However, the longitudinal pilots reported that the pitch damping and longitudinal control were only slightly degraded, and the longitudinal flying qualities remained satisfactory with no stability or control problems evident. Upon further increasing the angle of attack to approximately 20°, the wool surface tufts indicated that the inboard portion of the wing, including that portion of the wing directly ahead of the propeller disk, was stalled while the outer wing panels were experiencing spanwise flow. The longitudinal pilots reported a reduced level of longitudinal stability and an increased pilot work load; however, they felt that the overall longitudinal flying qualities were acceptable.

The flight angle of attack was gradually increased from approximately 20° to an upper range of approximately 24° to 27°. The longitudinal pilots reported that the model was becoming increasingly unstable and that the model required a great deal of effort to fly. The pilots reported that the control effectiveness was reduced and that the pitch damping was significantly degraded. The model flights were terminated at $\alpha \approx 24°$ to 27° because of a loss of pitch control. As noted previously, flight tests of the configuration with either the outboard-wing leading-edge droop or the outboard Krüger flap showed similar results. However, the longitudinal pilots noted slightly better flying qualities at the higher angles of attack with the outboard Krüger flap.

The preceding results are found to be in good qualitative agreement with the variation of C_m versus α (fig. 8) and the elevator control effectiveness (fig. 9). The data of figures 8 and 9 show a nonlinear increase in C_m and a marked reduction in $C_{m_{\delta_e}}$ for angles of attack on the order of 24°.

Predicted lateral-directional flying qualities. Figures 28, 29, and 30 present dynamic lateral-directional stability requirements having application to the present class of configuration in the approach flight phase. (See ref. 13.) Also presented in the figures are predicted results for the present configurations based on the following: (1) analysis of the static and dynamic aerodynamic data of the present test, and (2) full-scale mass and inertias obtained using model free-flight values and the dynamic scaling relationships presented in reference 4. (The present model scale is assumed to be 0.175.)

Figure 28 presents the Dutch roll stability requirement in terms of the damping and natural frequency of the Dutch roll mode. As can be seen, prior to the stall the baseline configuration meets level 1 Cooper-Harper flying qualities requirements. However, for poststall conditions the reduction in roll damping results in an unstable Dutch roll mode, and therefore the configuration flying qualities are considered unacceptable. This result correlates well with the free-flight tests which, for the baseline configuration, were terminated at the stall angle of attack due to an abrupt wing drop and autorotative departure against full corrective controls. Results for the configuration with modified outboard-wing leading edges (and, consequently, improved roll damping, see fig. 20) show that even for relatively high angles of

attack (i.e., $\alpha = 22°$ with $C_L = 2.0$), adequate Dutch roll flying qualities are achieved.

Figure 29 presents the spiral-stability requirements in terms of the time to double (half) the spiral-mode amplitude. The results show that the baseline configuration will satisfy level 1 spiral-stability flying qualities requirements. Results are also presented for the configuration with modified wing leading edges operating at $\alpha = 22°$ with $C_L = 2.0$. As can be seen, the spiral mode becomes increasingly stable, apparently because of the increase in effective dihedral ($-C_{l_\beta}$) and the reduction in roll due to yaw (C_{l_r}).

Roll-flying mode qualities requirements, based on the roll-mode time constant, are presented in figure 30. The results show that prior to stall, the baseline configuration satisfies level 1 criteria. For angles of attack above the stall (corresponding to conditions with reduced roll damping), the baseline configuration is found to satisfy level 3 requirements and is fairly close to satisfying the requirement for level 2. As might be expected, based on the improved roll damping afforded by wing leading-edge devices, the modified configuration is found to exhibit satisfactory values for the roll-mode time constant. For example, figure 30 shows that for the configuration with modified wing leading edges at $\alpha = 22°$, the roll-mode time constant is close to satisfying level 1 Cooper-Harper criteria.

Evaluation of lateral-directional flying qualities. For angles of attack below the stall, the lateral-directional pilots stated that the baseline configuration exhibited satisfactory flying qualities. The pilots remarked that the configuration had good roll and yaw control and sufficient roll and yaw damping without any form of artificial stabilization. Model free-flight tests conducted with artificial roll and yaw damping via rate feedbacks to the aileron and rudder (see fig. 3(b)) proved such concepts unnecessary.

As noted previously, the model free-flight tests of the baseline configuration were terminated at the stall angle of attack because of an abrupt wing drop and autorotative departure against full corrective controls. The wing drop is a result of an asymmetric rolling moment that occurs at the stall angle of attack. (See fig. 13.) This asymmetric rolling moment is a characteristic associated with wings that exhibit an abrupt stall. (See fig. 5.) The autorotative tendency is a result of reduced roll damping (see fig. 14), and the ineffectiveness of corrective controls is a result of reduced aileron effectiveness (see fig. 12).

For the configuration with either the outboard-wing leading-edge droop or the outboard Krüger flap, the lateral-directional pilots remarked that the model was fairly easy to fly up to the highest angle of attack considered (i.e., $\alpha \approx 24°$ to $27°$). The pilots stated that the configuration having modified outboard leading edges had good inherent lateral-directional stability and satisfactory lateral-directional control. The pilots reported, however, that the configuration with the outboard Krüger flap had improved roll damping and roll control, relative to the configuration with the outboard droops.

As noted in a previous section of this report, for the configurations with modified outboard-wing leading edges, the inboard portion of the wing showed evidence of intermittent stall for $\alpha \approx 16°$. Upon increasing the free-flight angle of attack to approximately 20°, the inboard portion of the wing stalled and the outboard wing panels developed a spanwise flow. Furthermore, the spanwise flow on the outboard wing panels was found to increase as the angle of attack increased from approximately 20° to 27°. Although the outboard wing panels were experiencing full spanwise flow, the force test data indicate that the outboard wing panel remains effective. For example, the lateral stability derivative C_{l_β} continues to increase with increasing α (see fig. 16), and the aileron remains effective for producing roll control (see fig. 18) up to the highest test angle of attack considered (i.e., $\alpha = 28°$). These results are in good agreement with the model free-flight test results.

Force test results for the directional stability and control characteristics are also found to be in good qualitative agreement with the model free-flight test results. For example, the directional stability derivative C_{n_β} shows that the configuration maintains directional stability (see fig. 16), and the rudder effectiveness derivative $C_{n_{\delta_r}}$ shows that the rudder remains effective for producing yaw control (see fig. 17) up to the highest angle of attack considered (i.e., $\alpha = 28°$). It should be noted that directional stability and rudder effectiveness are somewhat influenced by thrust. (See figs. 16 and 17, respectively.) However, for the symmetric model free-flight tests, the thrust coefficient was typically in excess of the $T_c' = 0.2$ value for which the static force tests were conducted, and therefore the static test data are generally representative of the stability characteristics for the free-flight test condition.

Evaluation of engine-out roll and yaw trim. Model free-flight tests were conducted to explore engine-out flight conditions. Tests were limited to the model configuration employing the outboard-wing leading-edge droop at an assumed approach angle of attack of approximately 12°.

Free-flight tests showed that the model could not achieve yaw trim while holding $\beta = 0°$. The

lateral-directional pilot was able to achieve engine-out yaw trim for only a combination of sideslipped conditions (corresponding to a "crabbed approach") with $\beta \approx 10°$ and with the maximum rudder deflection increased from 20° to 25°. In this trim condition the rudder was fully deflected and the lateral-directional pilot reported that there was insufficient rudder available for directional control. The pilot further noted that although he could achieve engine-out roll trim, the intermittent or unsteady nature of the wing stall on the side of the inoperative engine resulted in an abrupt roll-off tendency that required an excessive pilot work load to control.

As a matter of research interest, an extension was added to the rudder that increased the rudder chord and consequently increased the rudder area by approximately 65 percent. The increase in rudder chord was sufficient to position the rudder, when deflected, in the propeller slipstream. For these conditions, the pilot reported that the directional control was significantly improved; however, he still experienced an excessive work load because of the intermittent or unsteady stall (and subsequent wing drop) of the wing on the side of the inoperative engine.

The foregoing model free-flight test results are in good qualitative agreement with the results of analysis as presented in figures 24 and 26, which are based on a linear analysis of the static force test data. It should be further noted that the intermittent or unsteady nature of the stall is not reflected by the static data that serve as input for the analysis. Therefore, the analytical results presented provide an optimistic assessment of the engine-out trim condition.

Summary of Results

An investigation was conducted to determine the low-speed flight dynamic behavior of a representative, advanced turboprop business/commuter aircraft concept. The investigation was conducted using model free-flight tests in the Langley 30- by 60-Foot Tunnel. In support of the free-flight tests, conventional static, dynamic, and free-to-roll oscillation tests were performed. The results of this investigation are summarized as follows:

1. The model free-flight test pilots commented that for angles of attack below the stall, the baseline configuration was stable and easy to fly. The pilots found that the basic airframe had satisfactory damping about all three axes and was responsive to longitudinal and lateral-directional control inputs.

2. At the stall angle of attack the free-flight tests of the baseline configuration were terminated because of an abrupt wing drop and autorotative departure against full corrective roll control. Conventional wind-tunnel tests showed that the wing drop was due to an abrupt asymmetric wing stall that produced a pronounced rolling moment.

3. Free-flight tests of the configuration with modified leading edges (either outboard-wing leading-edge droops or outboard Krüger flaps) showed a significant improvement in roll control and a substantial increase in roll damping. For an angle of attack α on the order of 20°, the pilots indicated that the overall flying qualities were acceptable and no significant stability or control problems were evident for either the longitudinal or lateral-directional axes.

4. Free-flight tests of the configuration with the modified leading edges were terminated at $\alpha = 24°$ to 27° because of a loss of pitch control. Static force tests showed a consistent reduction in elevator effectiveness for an angle of attack of 24°.

5. Model free-flight tests conducted to explore engine-out trim and flight dynamics were limited to the model configuration employing outboard-wing leading-edge droops at an assumed approach angle of attack of approximately 12°. Free-flight tests showed that the model could not achieve yaw trim while holding the angle of sideslip β at 0°; also, engine-out yaw trim could only be achieved for sideslipped conditions with $\beta \approx 10°$ and with the rudder fully deflected to 25°. In this trim condition the rudder was fully deflected and there was insufficient rudder available for directional control. The pilot further noted that although he could achieve engine-out roll trim, the intermittent or unsteady nature of the wing stall on the side of the inoperative engine resulted in an abrupt roll-off tendency that required an excessive pilot work load to control.

NASA Langley Research Center
Hampton, VA 23665-5225
March 2, 1990

References

1. Goldsmith, I. M.: *A Study To Define the Research and Technology Requirements for Advanced Turbo/Propfan Transport Aircraft.* NASA CR-166138, 1981.
2. Coe, Paul L., Jr.; Applin, Zachary T.; and Williams, Louis J.: Stability and Control Results for Advanced Turboprop Aft-Mount Installations. *SAE 1984 Transactions,* Volume 93, Soc. of Automotive Engineers, Inc., c.1985, pp. 6.256–6.263. (Available as SAE Paper 841479.)
3. Dunham, Dana Morris; Gentry, Garl L., Jr.; Manuel, Gregory S.; Applin, Zachary T.; and Quinto, P. Frank: *Low-Speed Aerodynamic Characteristics of a Twin-Engine General Aviation Configuration With Aft-Fuselage-Mounted Pusher Propellers.* NASA TP-2763, 1987.

4. Chambers, Joseph R.; Bowman, James S., Jr.; and Malcolm, Gerald N.: Stall/Spin Test Techniques Used by NASA. *Stall/Spin Problems of Military Aircraft*, AGARD-CP-199, June 1976, pp. 13-1–13-12.

5. Chambers, Joseph R.; and Grafton, Sue B.: *Static and Dynamic Longitudinal Stability Derivatives of a Powered 1/9-Scale Model of a Tilt-Wing V/STOL Transport.* NASA TN D-3591, 1966.

6. Brandon, Jay M.; and Nguyen, Luat T.: Experimental Study of Effects of Forebody Geometry on High Angle of Attack Static and Dynamic Stability. AIAA-86-0331, Jan. 1986.

7. Staff, Langley Research Center: *Exploratory Study of the Effects of Wing-Leading-Edge Modifications on the Stall/Spin Behavior of a Light General Aviation Airplane.* NASA TP-1589, 1979.

8. Newsom, William A., Jr.; Satran, Dale R.; and Johnson, Joseph L., Jr.: *Effects of Wing-Leading-Edge Modifications on a Full-Scale, Low-Wing General Aviation Airplane—Wind-Tunnel Investigation of High-Angle-of-Attack Aerodynamic Characteristics.* NASA TP-2011, 1982.

9. Stough, H. Paul; DiCarlo, Daniel J.; and Stewart, Eric C.: Wing Modification for Increased Spin Resistance. SAE Paper No. 830720, Apr. 1983.

10. Chambers, Joseph R.; and Stough, H. Paul, III: Summary of NASA Stall/Spin Research for General Aviation Configurations. AIAA-86-2597, Sept. Oct. 1986.

11. Yip, Long P.; King, Patrick M.; Muchmore, C. Byram; and Davis, Pat: Exploratory Wind Tunnel Investigations of the Low-Speed Stability and Control Characteristics of Advanced General Aviation Configurations. AIAA-86-2596, Sept. Oct. 1986.

12. Etkin, Bernard: *Dynamics of Flight.* John Wiley & Sons, Inc., c.1959, p. 232.

13. *Military Specification—Flying Qualities of Piloted Airplanes.* MIL-F-8785C, Nov. 5, 1980. (Supersedes MIL-F-8785B, Aug. 7, 1969.)

14. Shomber, H. A.; and Gertsen, W. M.: Longitudinal Handling Qualities Criteria: An Evaluation. AIAA Paper No. 65-780, Nov. 1965.

Table I. Geometric and Mass Characteristics of Model

(a) Geometric characteristics

Fuselage:	
Body station of fuselage nose, in.	3.129
Length, ft	7.833
Maximum diameter, in.	11.2
Wing:	
Area (trapezoidal reference), ft^2	9.869
Span, ft	9.072
Quarter-chord sweep, deg	1.41
Aspect ratio	8.3
Taper ratio (trapezoidal reference)	0.35
Mean aerodynamic chord, in.	14.172
Dihedral, deg	4
Root incidence, deg	3.181
Body station of wing leading edge at root, in.	40.376
Body station of moment reference center, in.	48.38
Side-of-body airfoil chord, in.	22.05
Leading-edge-break airfoil chord, in.	15.924
Tip airfoil chord, in.	6.452
Horizontal tail:	
Area, ft^2	2.067
Span, ft	3.211
Aspect ratio	4.988
Quarter-chord sweep, deg	31.6
Dihedral, deg	−3.0
Taper ratio	0.35
Mean geometric chord, in.	8.324
Body station of tail leading edge at root, in.	93.999
Root airfoil chord, in.	11.431
Tip airfoil chord, in.	4.002
Vertical tail:	
Area, ft^2	2.016
Height, in.	18.223
Quarter-chord sweep, deg	50.0
Mean geometric chord, in.	16.259
Body station of tail leading edge at root, in.	77.195
Root airfoil chord, in.	19.909
Tip airfoil chord, in.	11.946
Pylon:	
Area, ft^2	1.948
Span (nacelle centerline to nacelle centerline), in.	26.74
Dihedral, deg	14.25
Body station of pylon leading edge at root, in.	61.49
Chord, in.	10.49
Propellers (single rotation):	
Tip diameter, in.	17.5
Maximum nacelle diameter, in.	5.67
Body station at propeller disk, in.	76.00

(b) Mass characteristics

Weight, lb	123
Moment of inertia:	
I_X, slug-ft^2	3.944
I_Y, slug-ft^2	16.096
I_Z, slug-ft^2	19.255

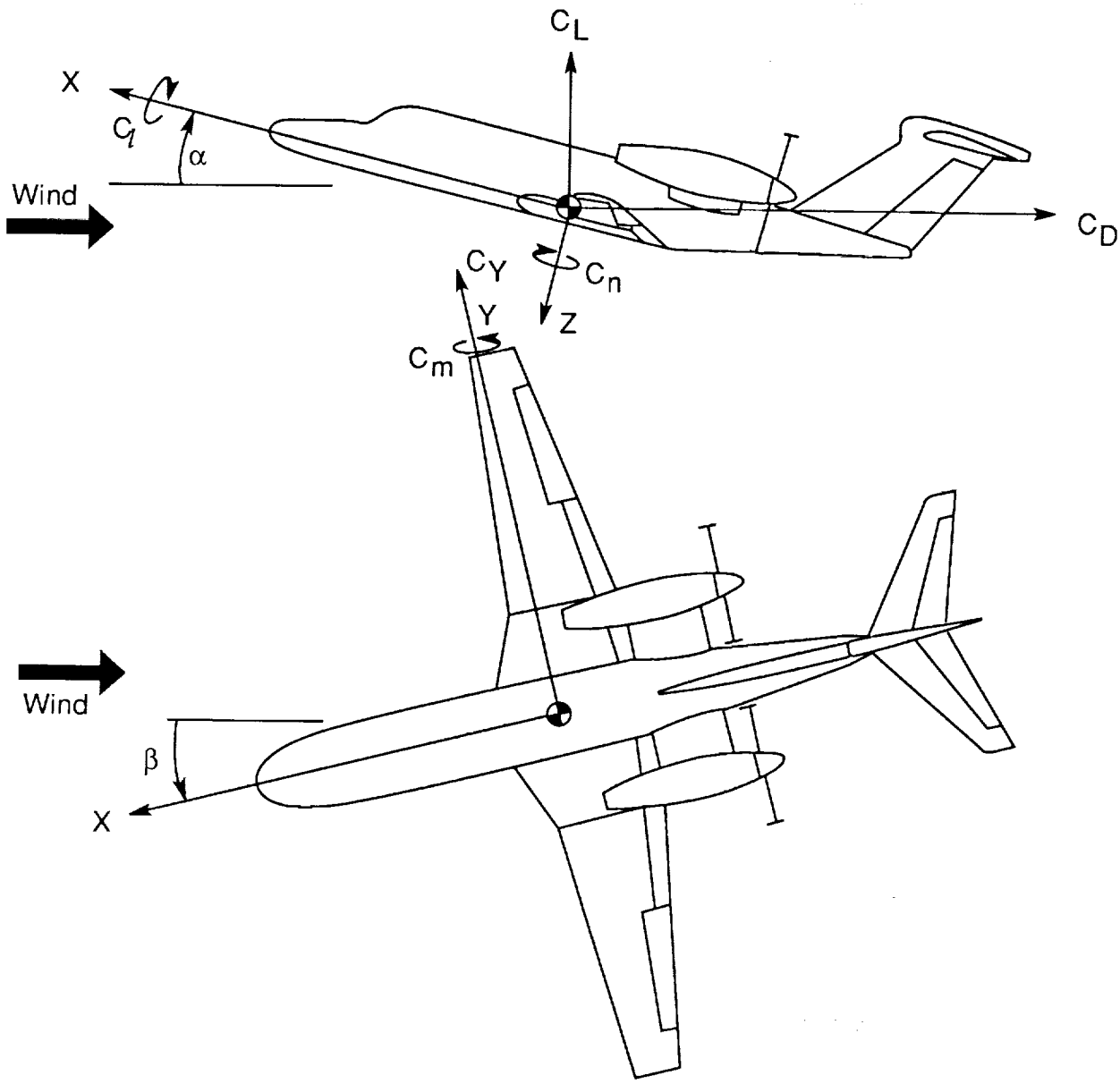

Figure 1. System of axes.

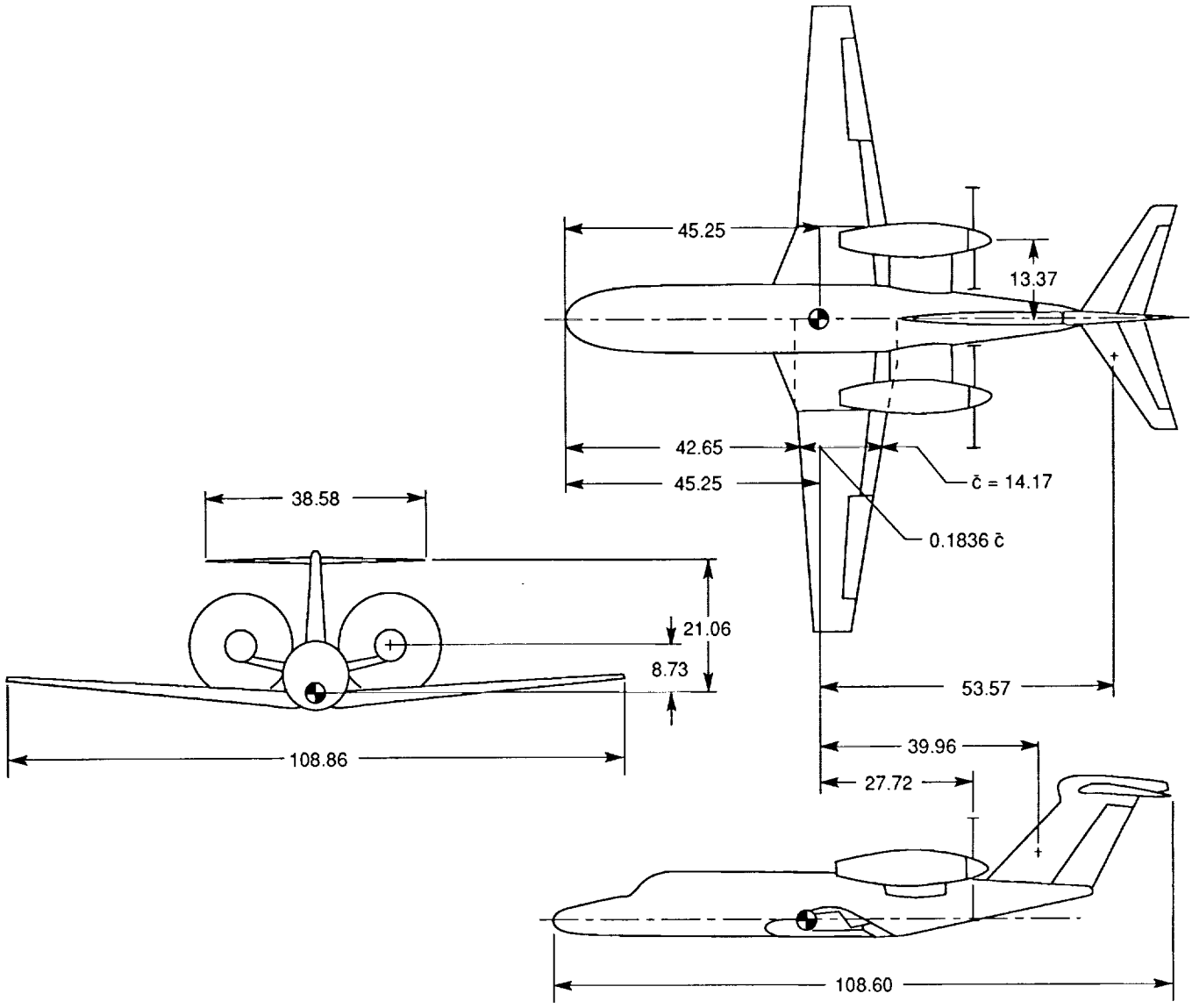

(a) Three-view sketch of model.

Figure 2. Geometric characteristics. Linear dimensions are given in inches.

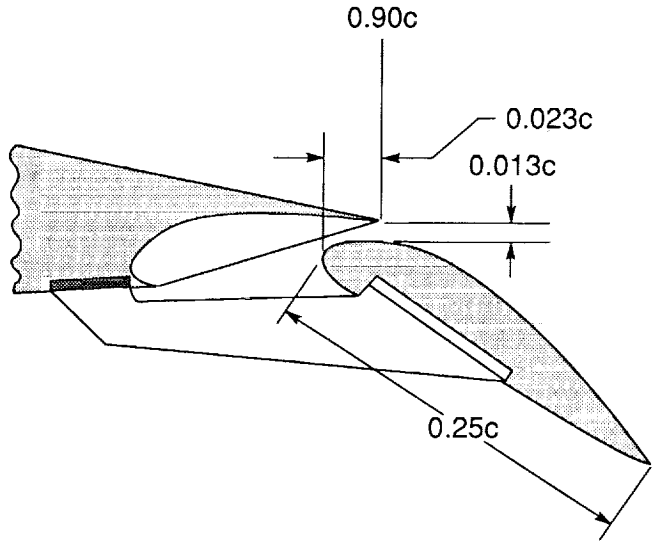

(b) Model trailing-edge flap. $\delta_f = 35°$.

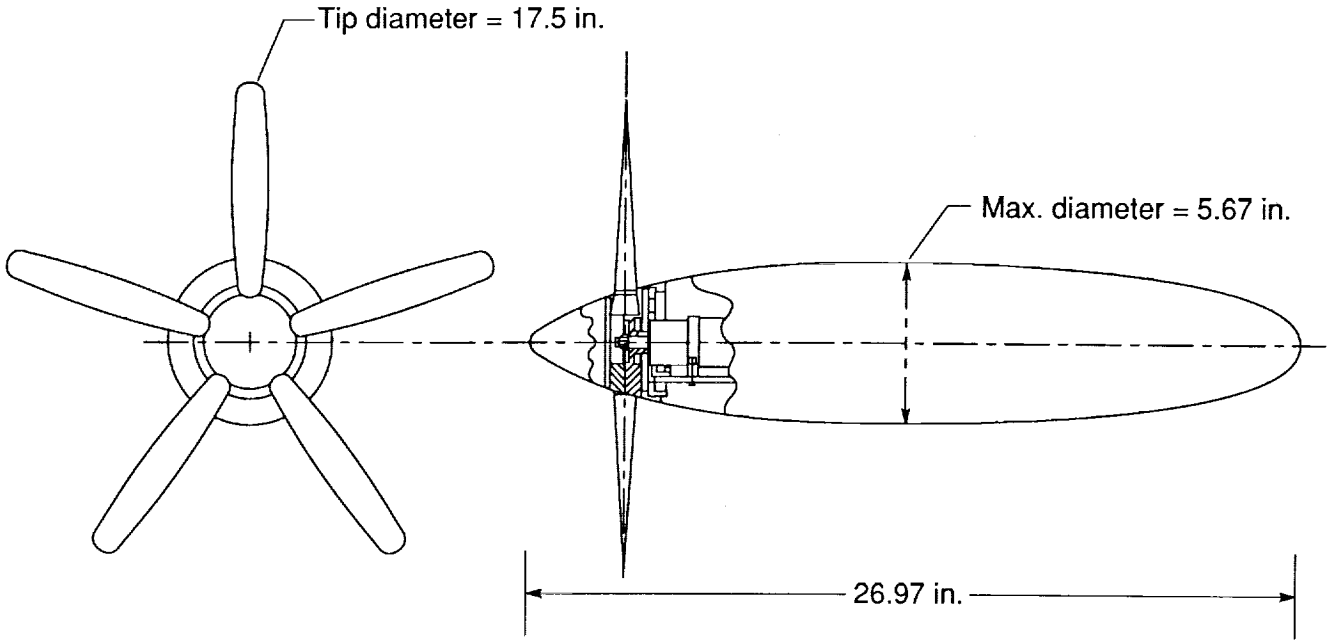

(c) Sketch of propeller and nacelle.

Figure 2. Continued.

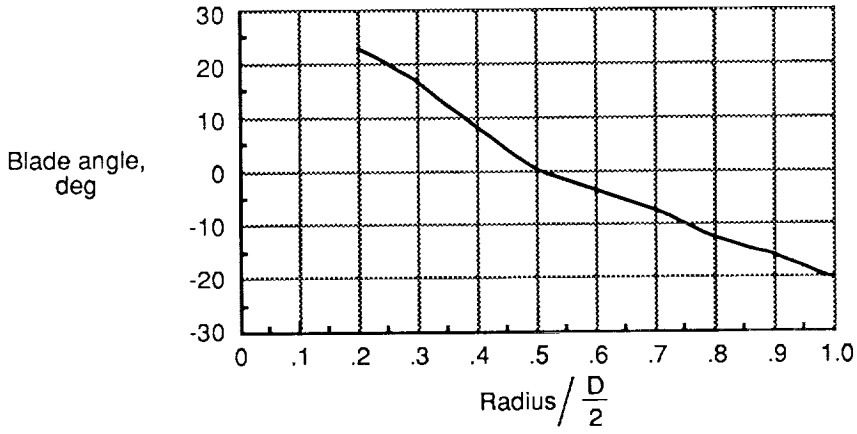

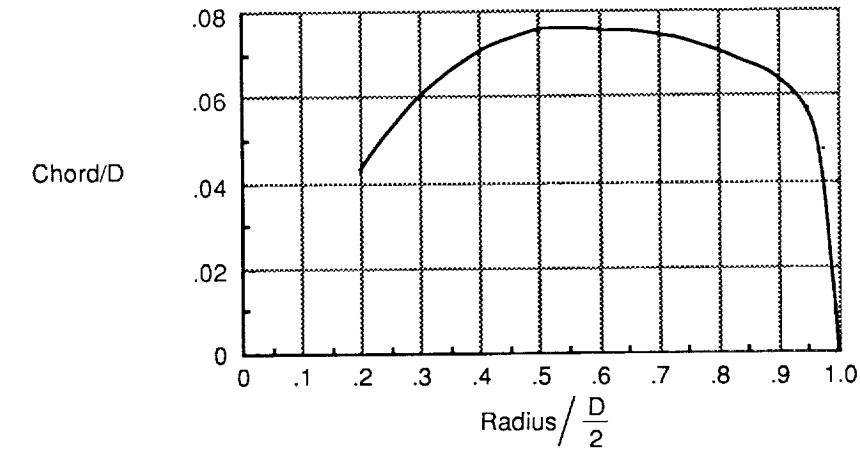

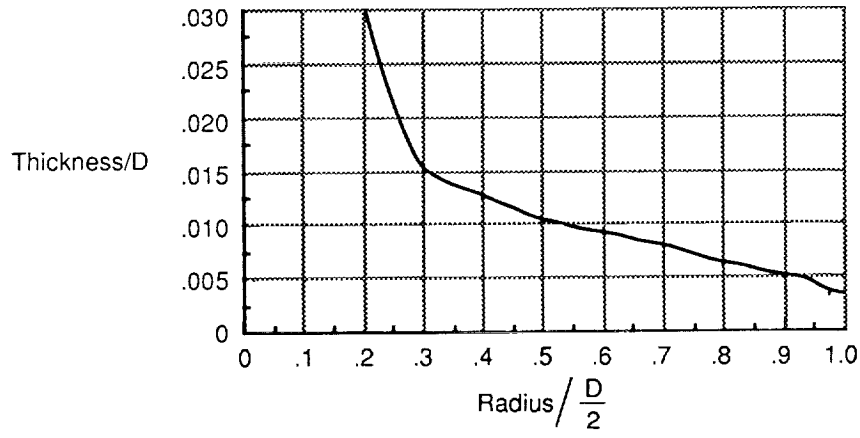

(d) Propeller blade coordinates.

Figure 2. Continued.

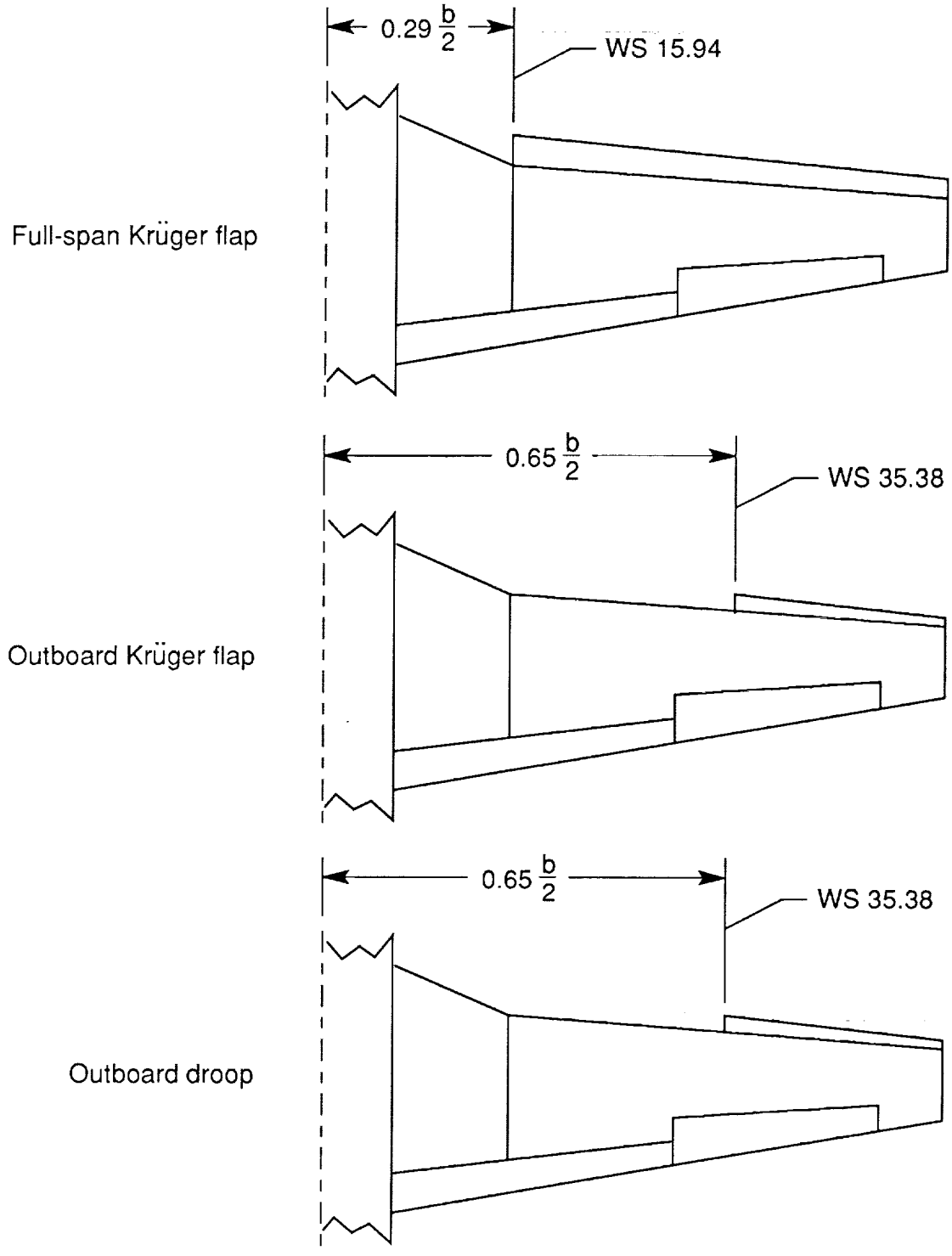

(e) Planform view of wing leading-edge devices.

Figure 2. Continued.

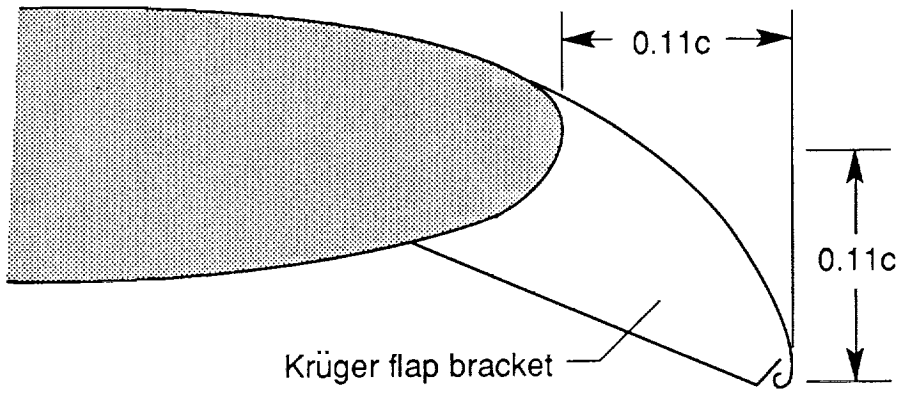

Inboard Krüger flap, WS 15.94

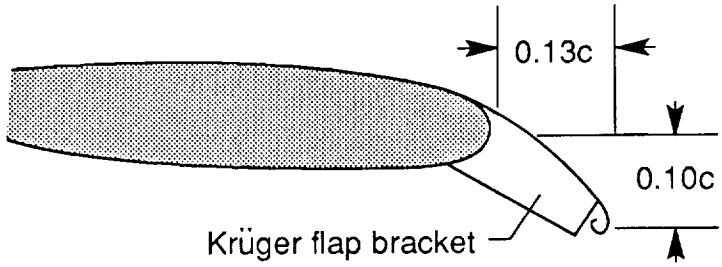

Outboard Krüger flap, WS 54.43

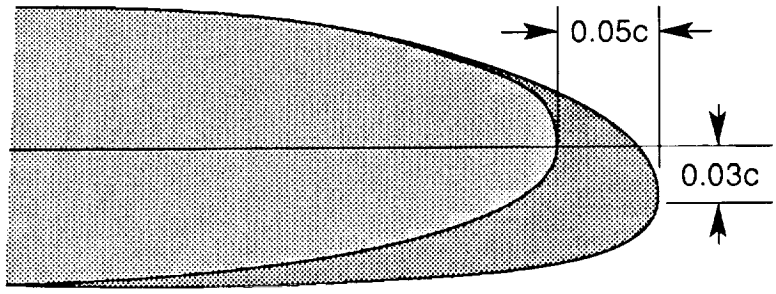

Outboard droop, all wing stations

(f) Wing leading-edge devices.

Figure 2. Concluded.

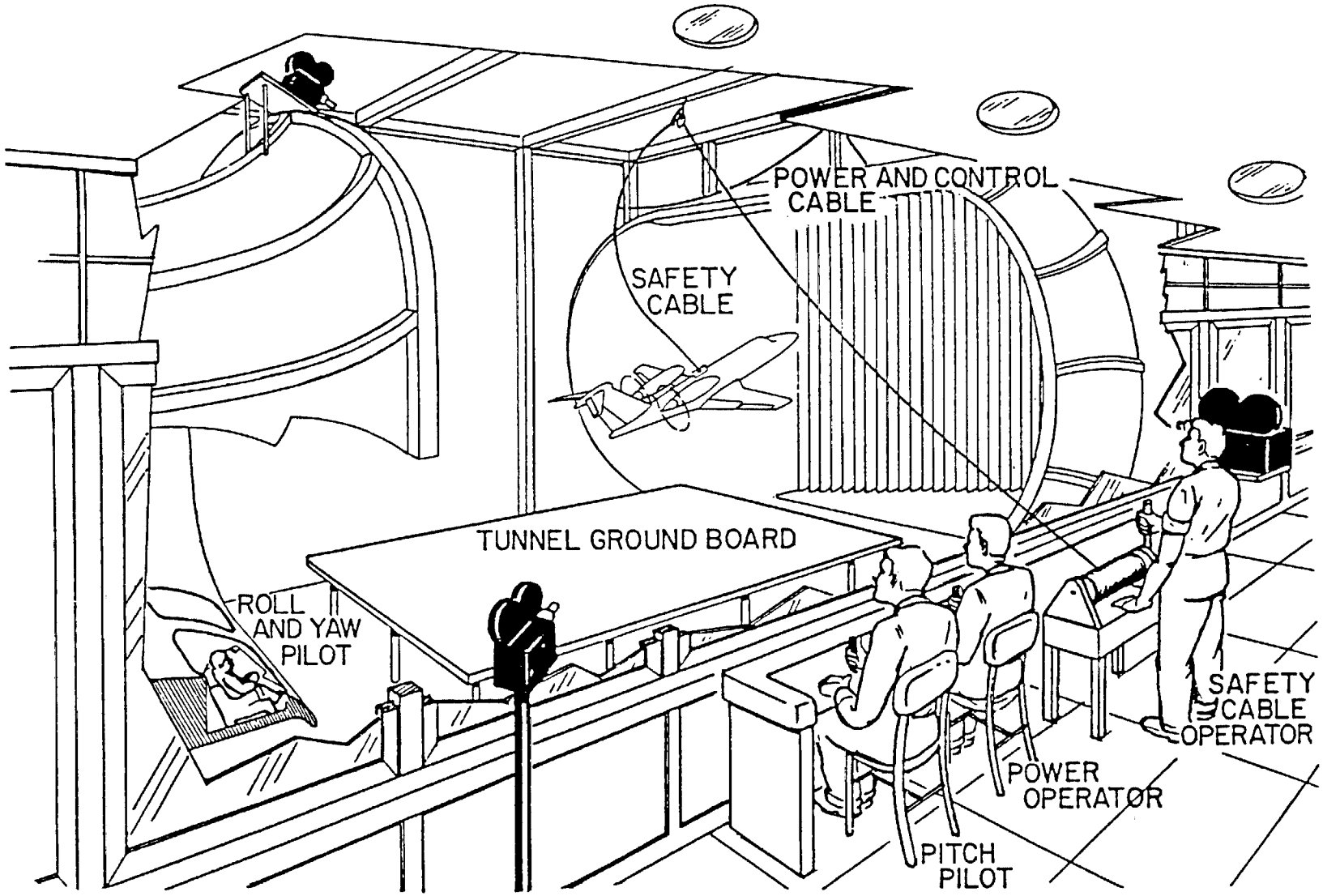

(a) Sketch of free-flight test setup.

Figure 3. Model test techniques in the Langley 30- by 60-Foot Tunnel.

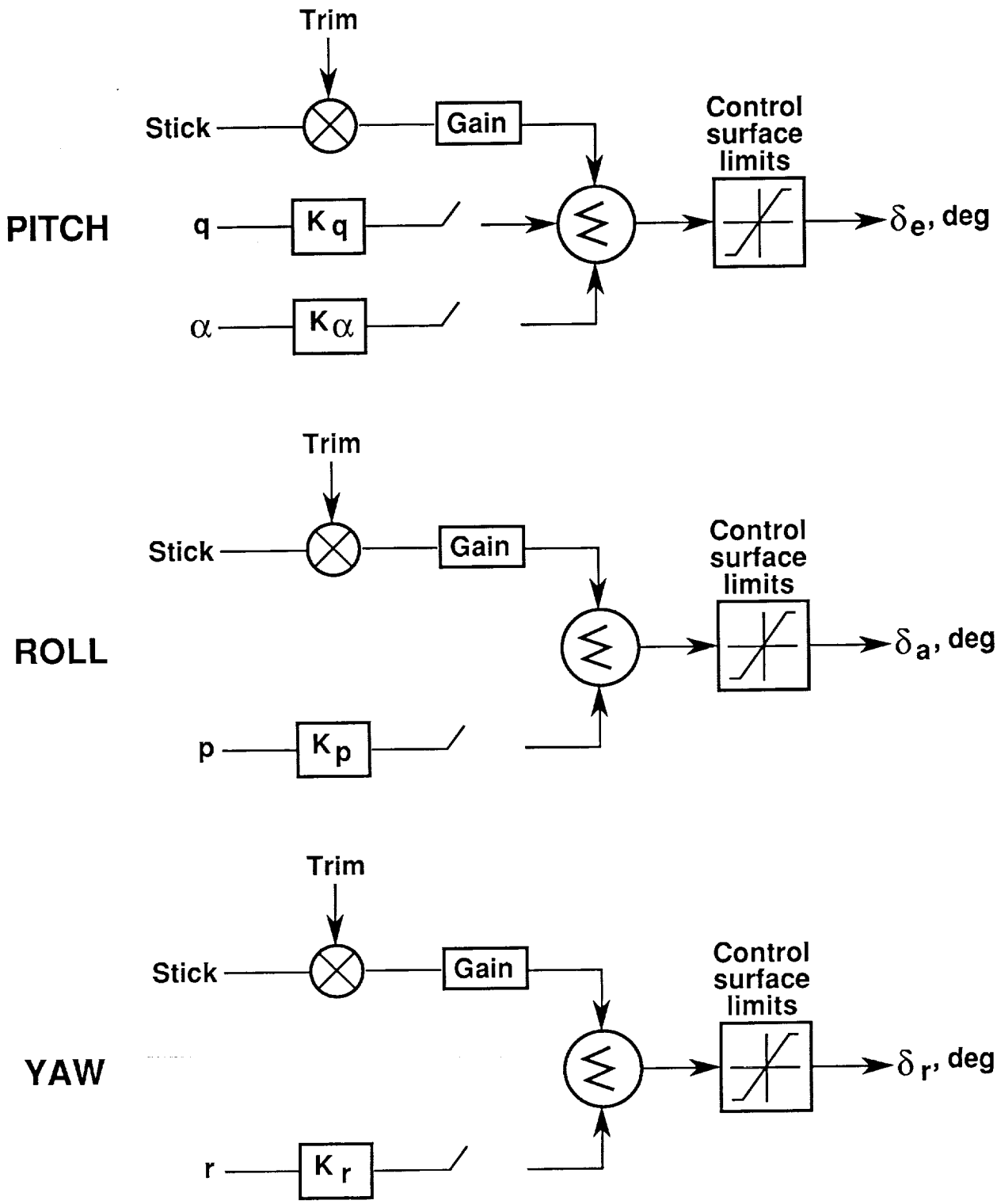

(b) Schematic of control system.

Figure 3. Continued.

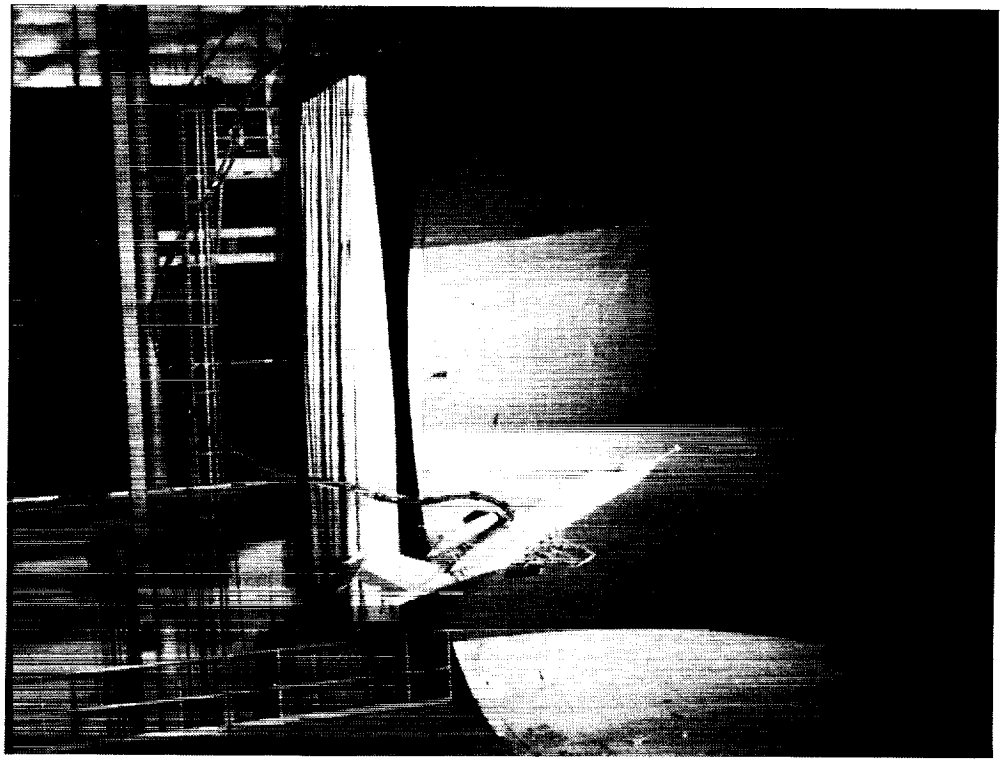

L-88-4421

(c) Photograph of model during free-flight tests.

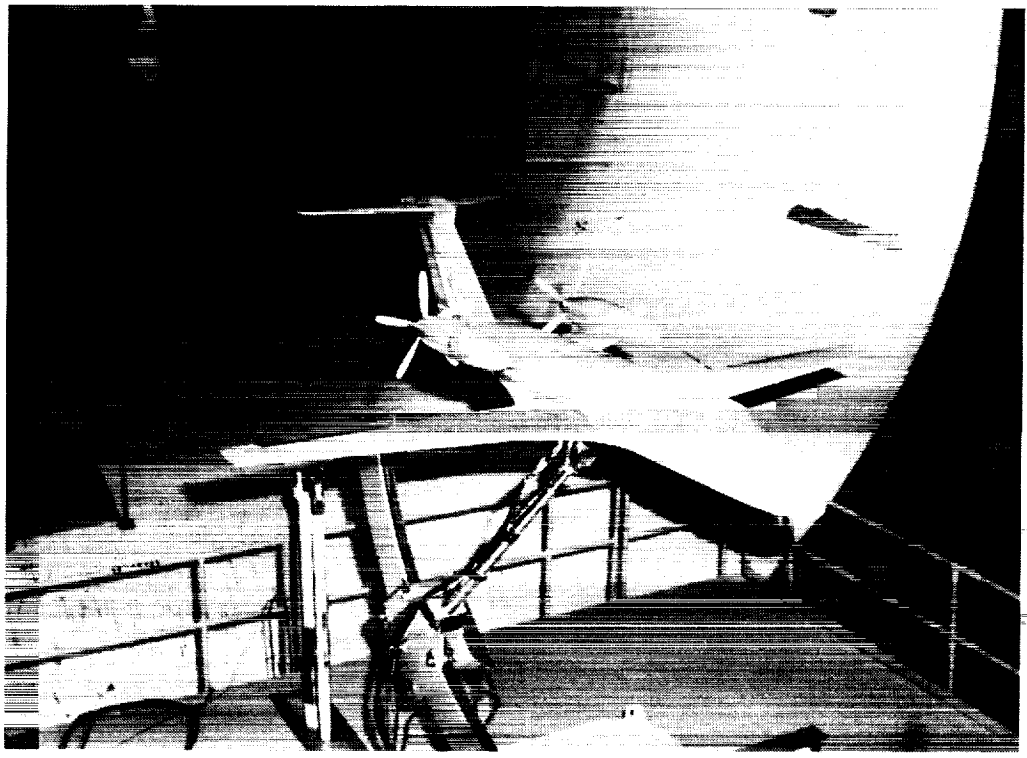

L-88-00780

(d) Photograph of model mounted for static tests.

Figure 3. Continued.

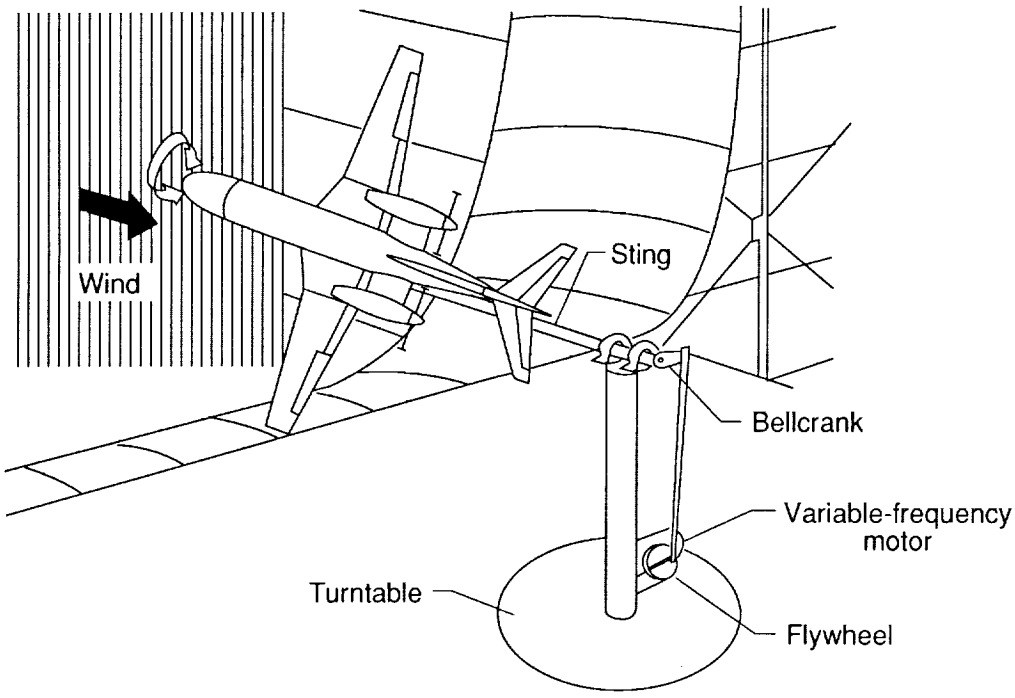

(e) Sketch of model mounted for forced-oscillation tests in roll.

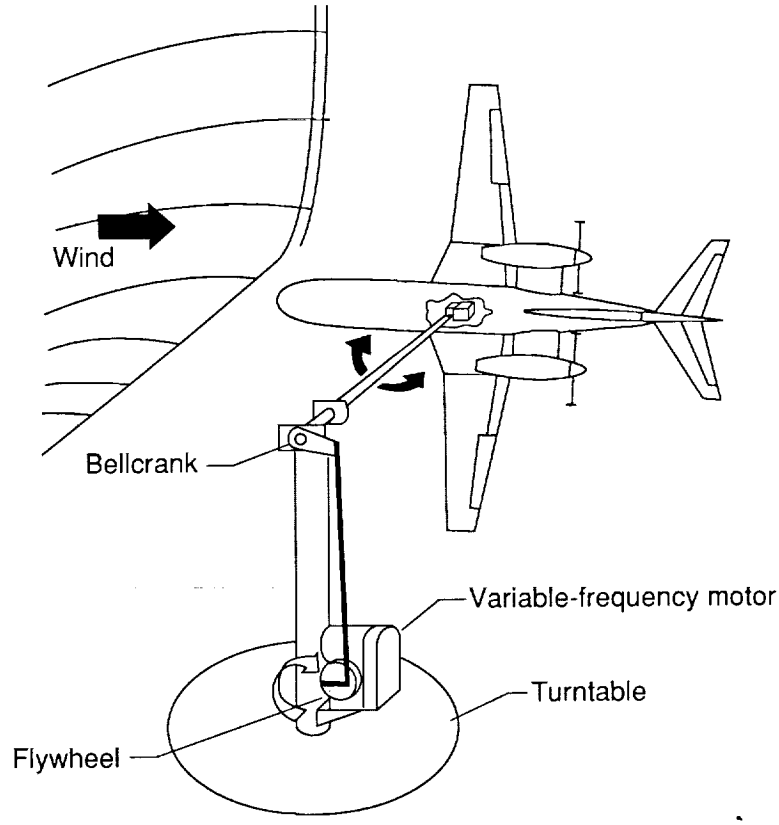

(f) Sketch of model mounted for forced-oscillation tests in yaw.

Figure 3. Continued.

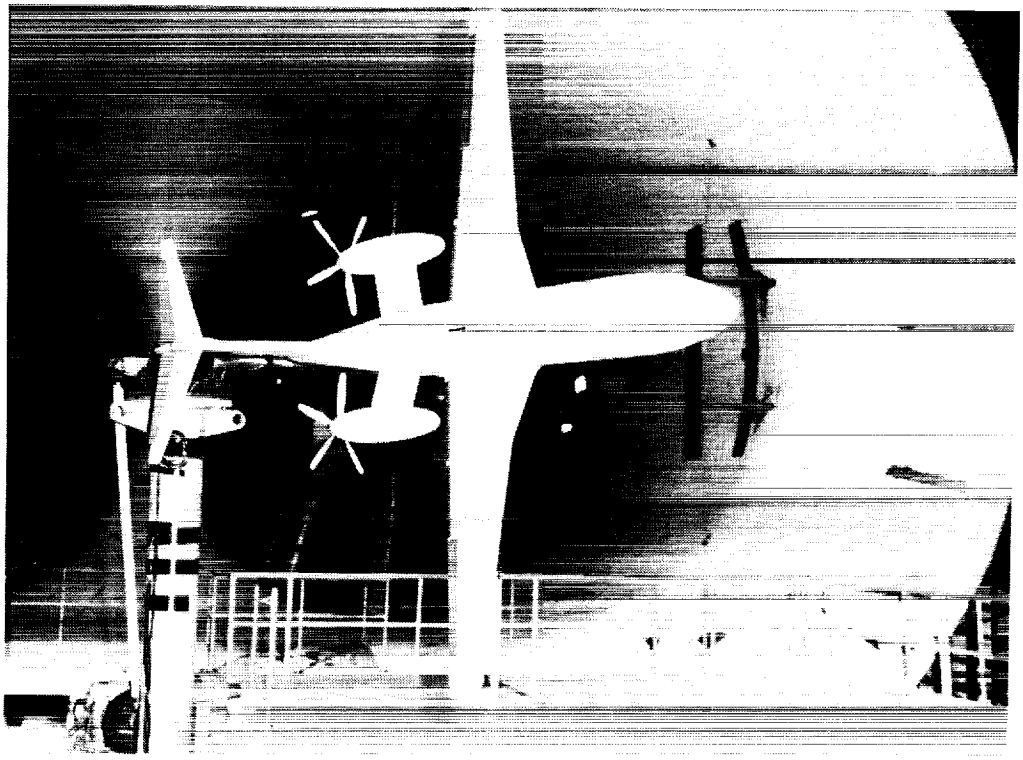

L-87-08902

(g) Photograph of model mounted for forced-oscillation tests in roll.

L-87-10617

(h) Photograph of model mounted for forced-oscillation tests in yaw.

Figure 3. Concluded.

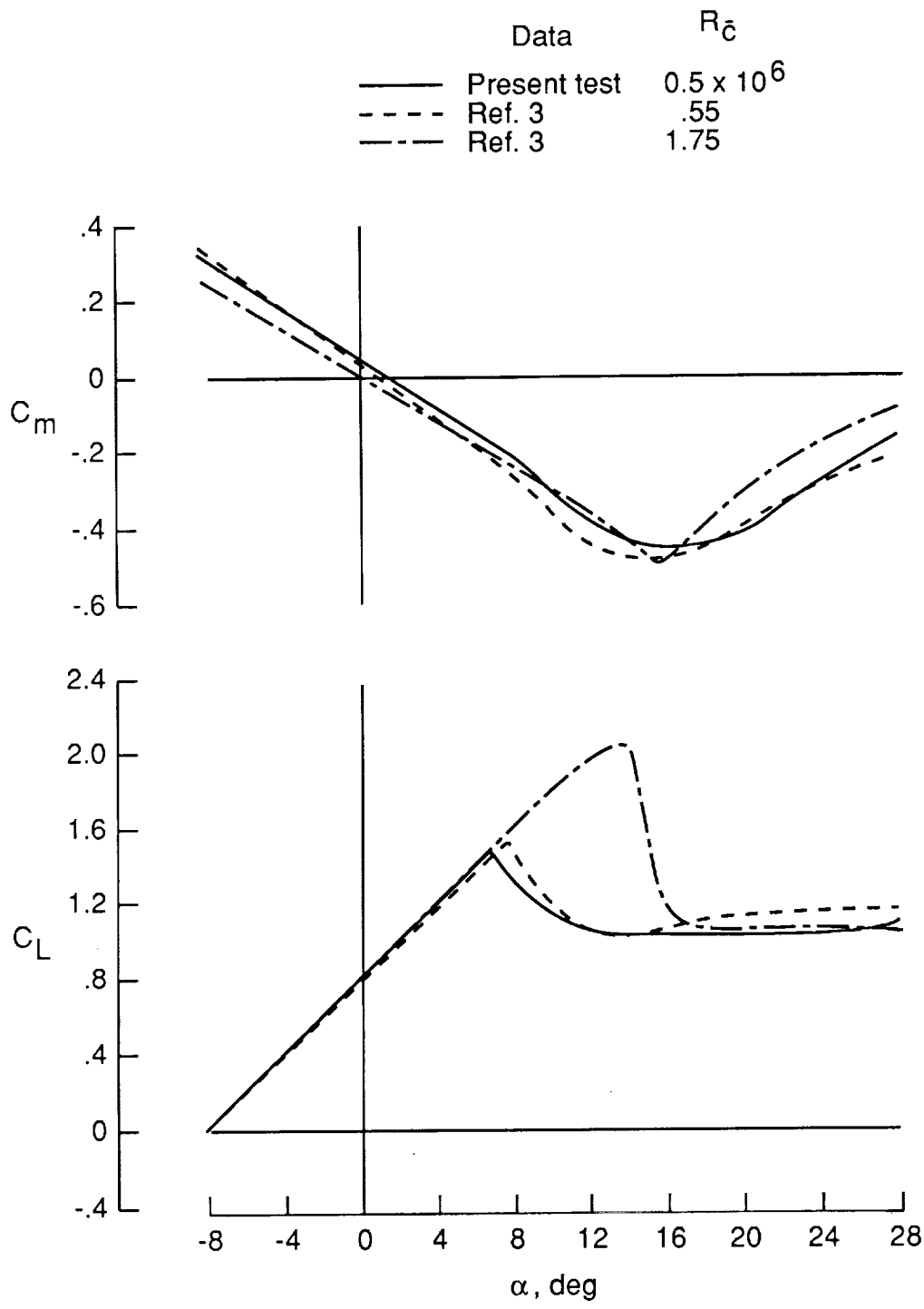

Figure 4. Longitudinal aerodynamic characteristics for complete baseline configuration. $\delta_f = 35°$; propellers windmilling.

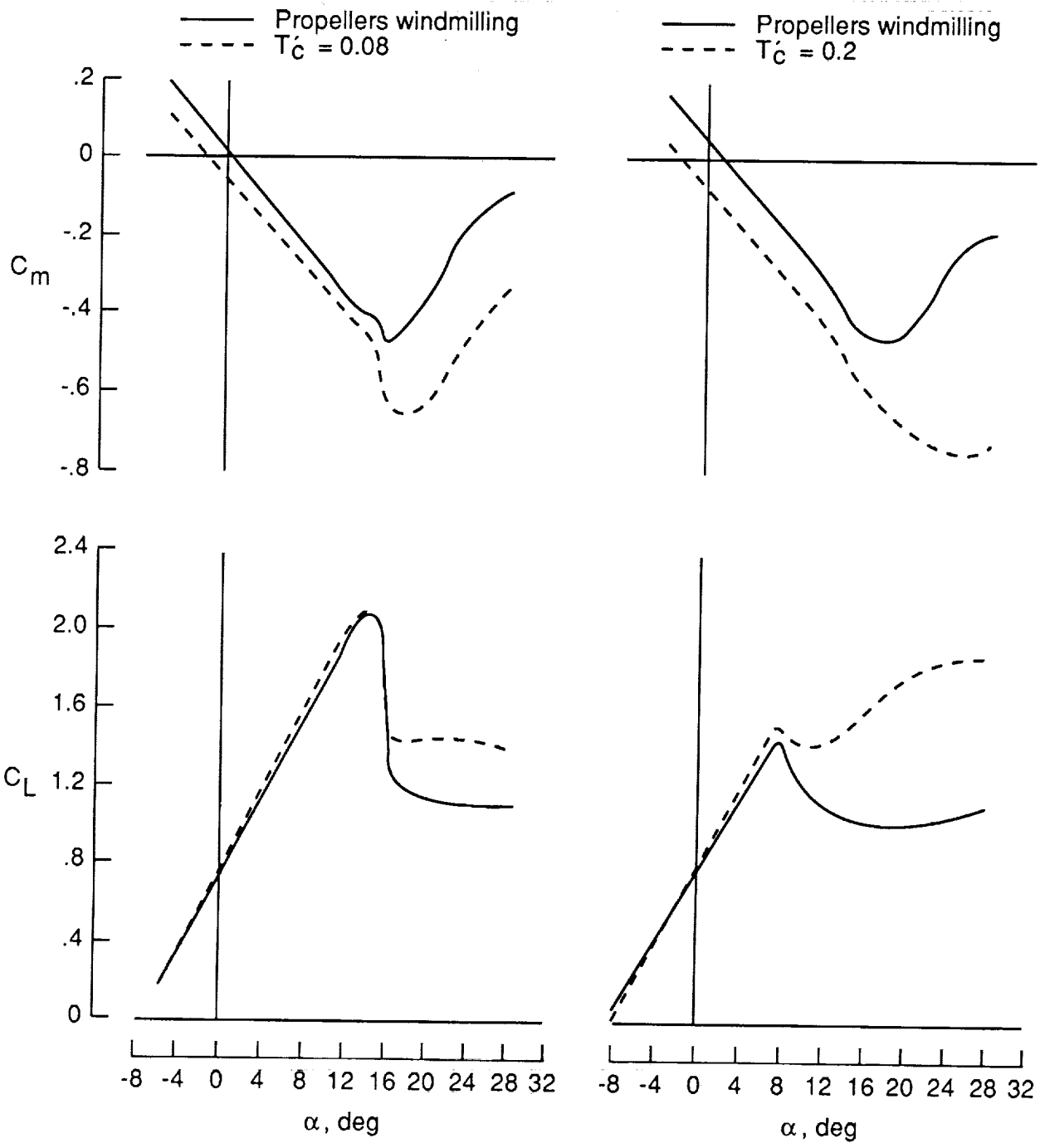

(a) Data from reference 3. $R_{\bar{c}} = 2.0 \times 10^6$.

(b) Data from present test. $R_{\bar{c}} = 0.5 \times 10^6$.

Figure 5. Effect of power on longitudinal aerodynamic characteristics. Baseline configuration; $\delta_f = 35°$.

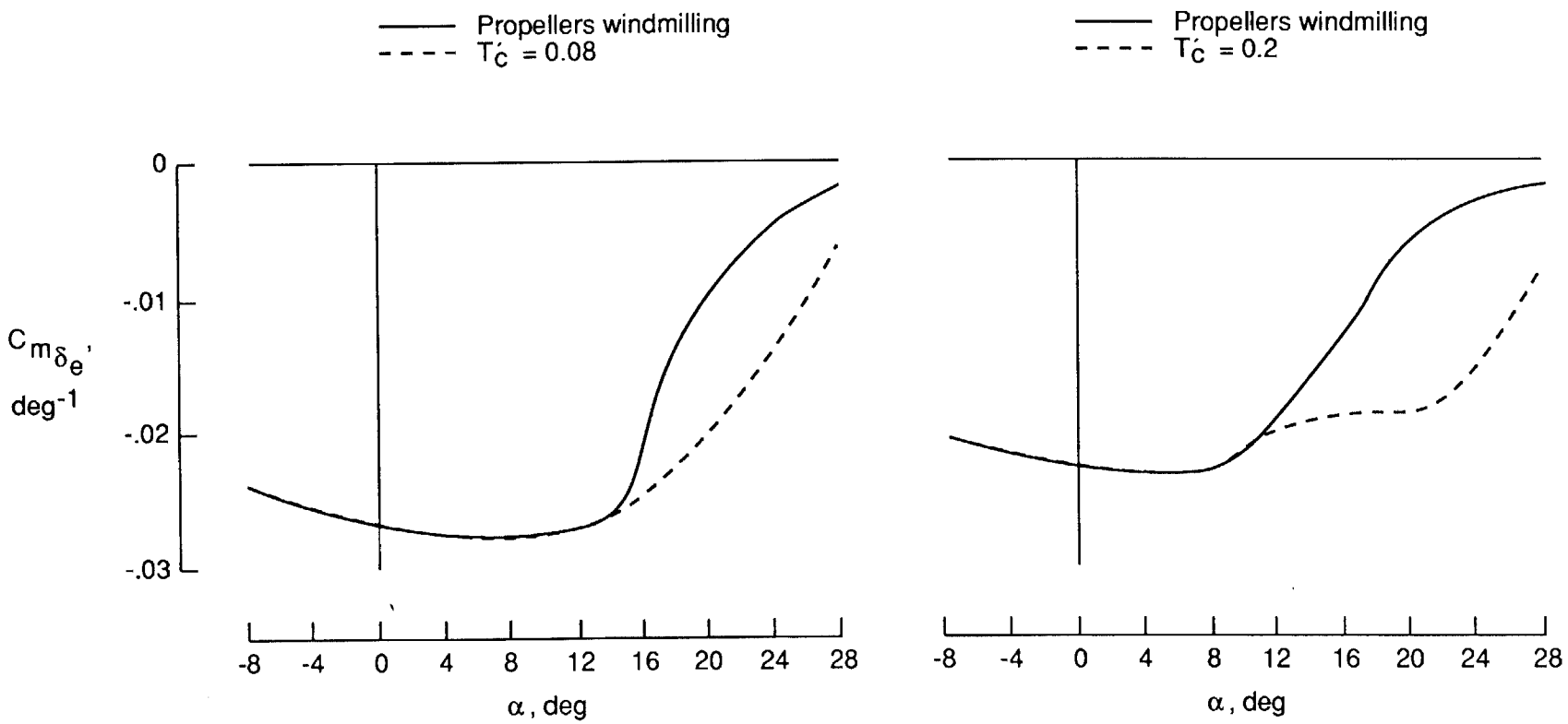

(a) Data from reference 3. $R_{\bar{c}} = 2.0 \times 10^6$.

(b) Data from present test. $R_{\bar{c}} = 0.5 \times 10^6$.

Figure 6. Effect of power on elevator effectiveness. Baseline configuration; $\delta_f = 35°$.

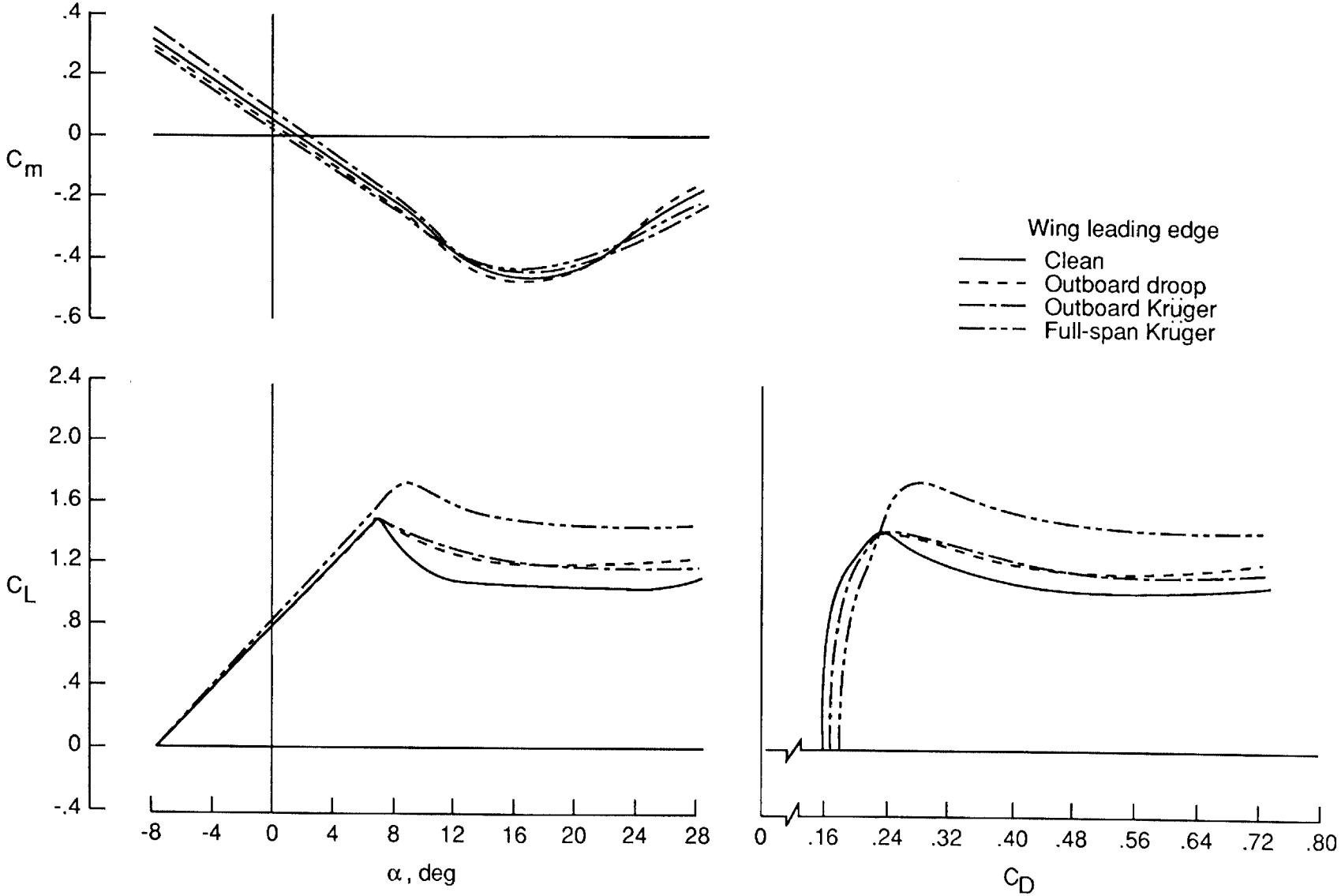

Figure 7. Effect of wing leading-edge devices on longitudinal aerodynamic characteristics. Baseline configuration; $\delta_f = 35°$; $T_c' = 0$; $R_{\bar{c}} = 0.5 \times 10^6$.

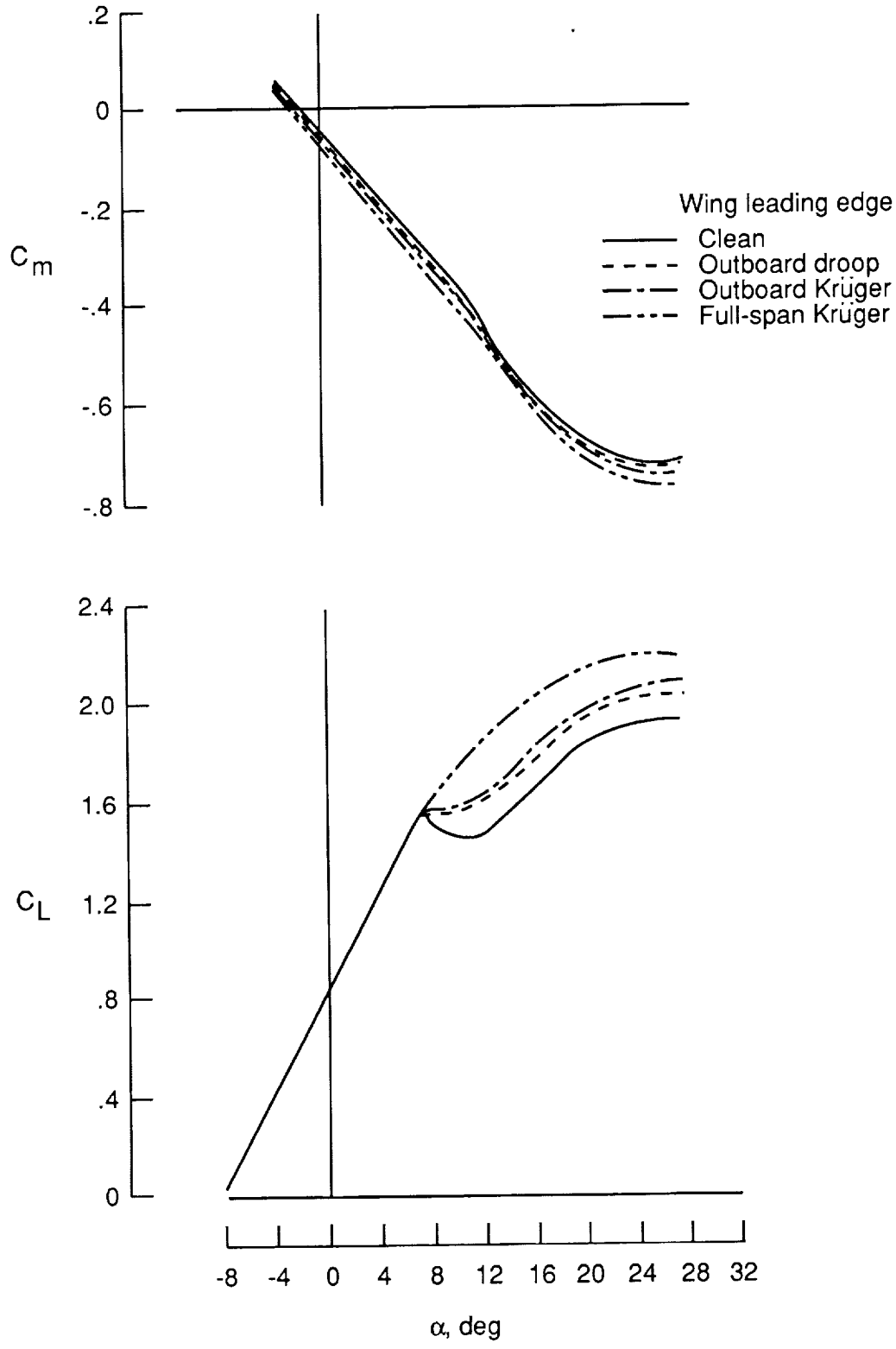

Figure 8. Effect of wing leading-edge devices on longitudinal aerodynamic characteristics. $\delta_f = 35°$; $T_c' = 0.2$.

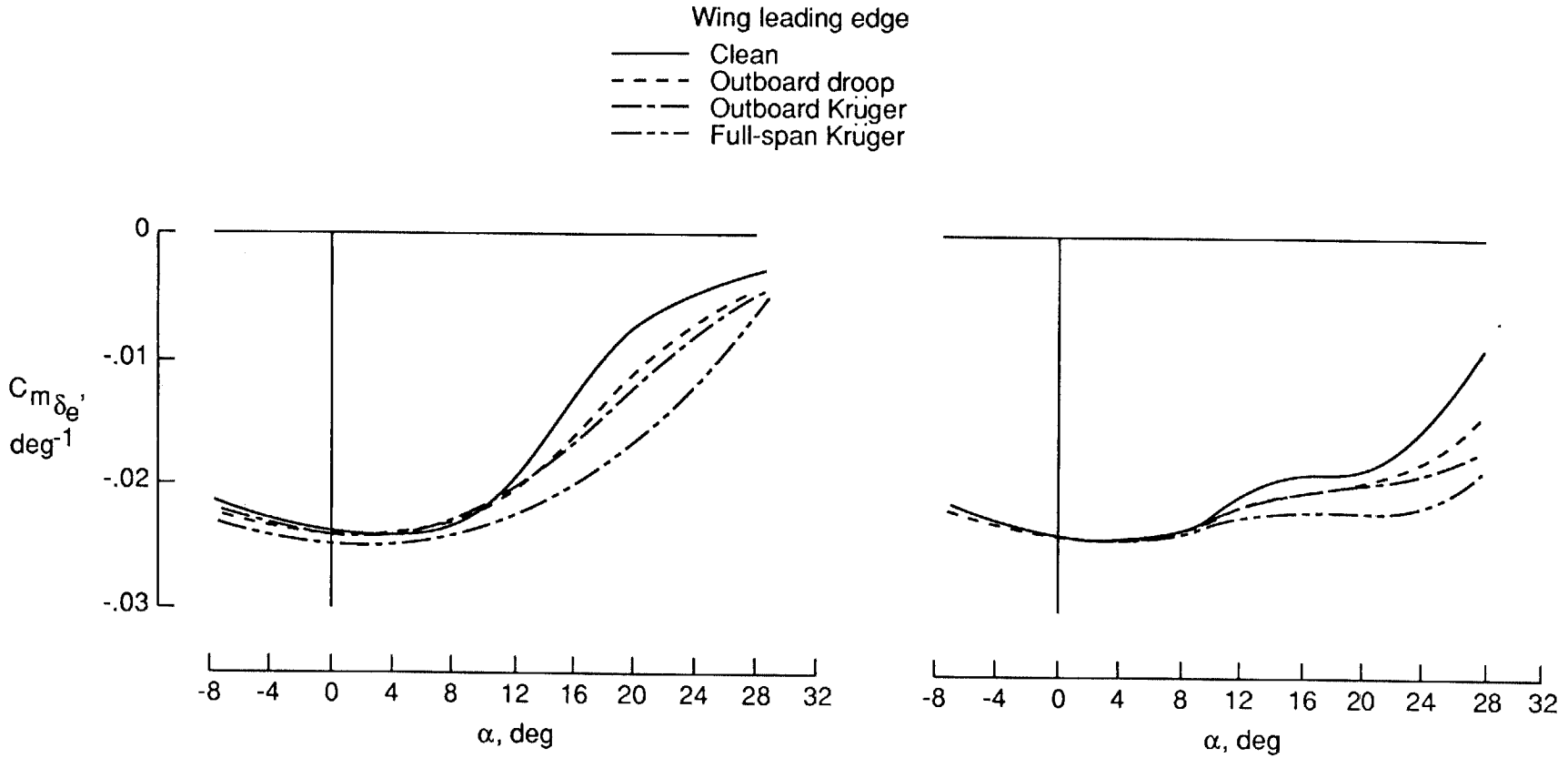

(a) $T_c' = 0$.

(b) $T_c' = 0.2$.

Figure 9. Effect of wing leading-edge devices on elevator effectiveness.

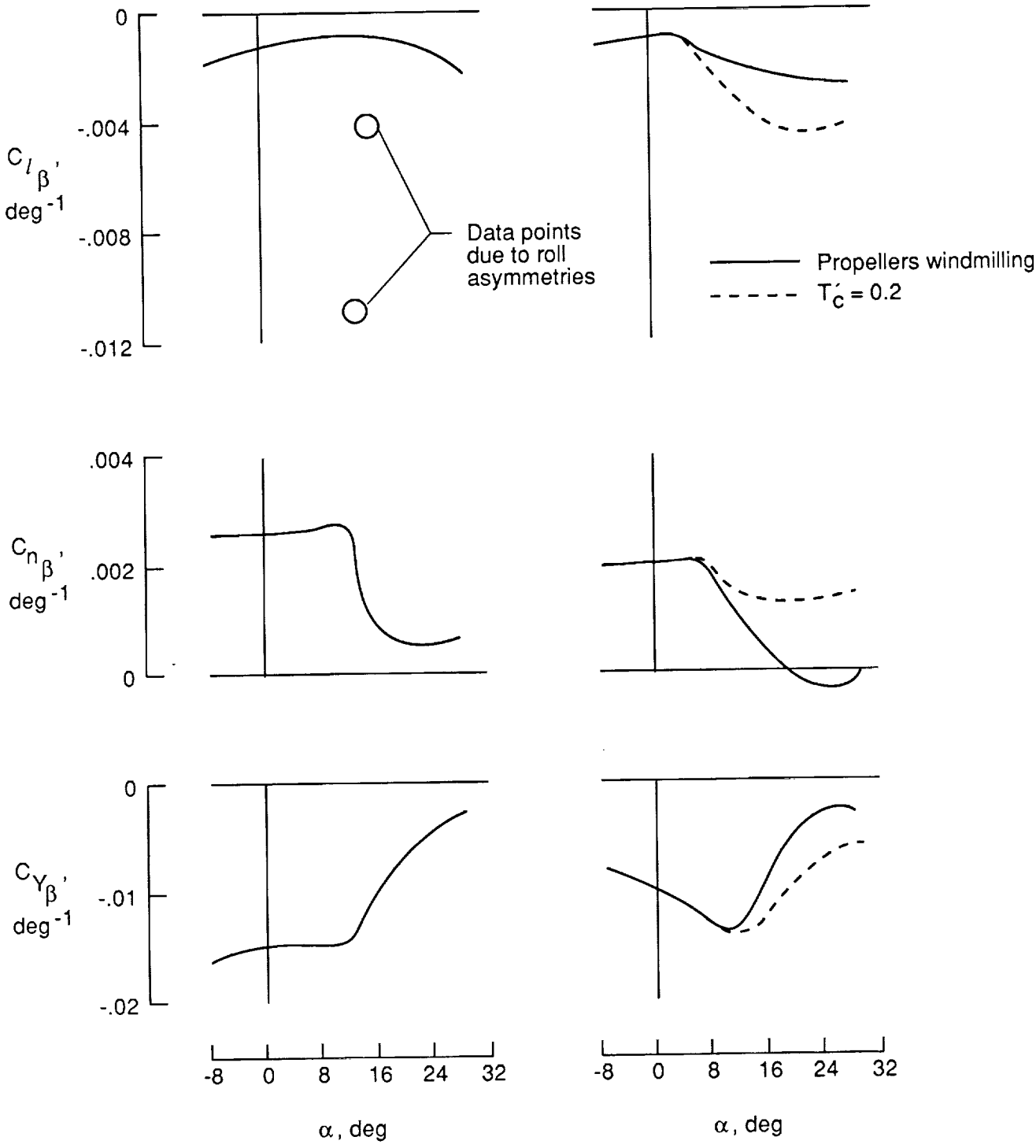

(a) Data from reference 3. $R_{\bar{c}} = 2.0 \times 10^6$.

(b) Data from present test. $R_{\bar{c}} = 0.5 \times 10^6$.

Figure 10. Effect of thrust on static lateral-directional stability characteristics. Baseline configuration.

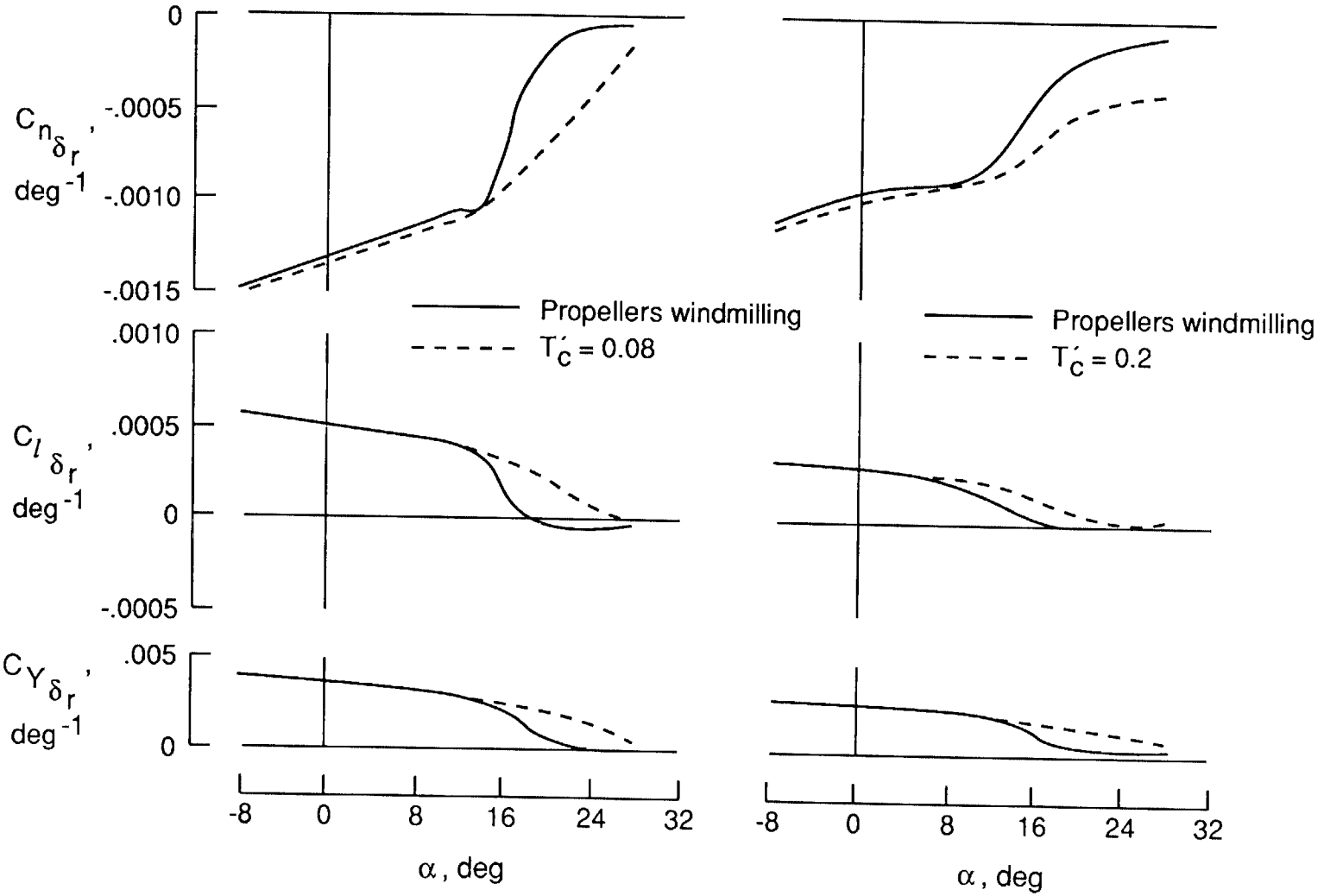

(a) Data from reference 3. $R_{\bar{c}} = 2.0 \times 10^6$.

(b) Data from present test. $R_{\bar{c}} = 0.5 \times 10^6$.

Figure 11. Effect of thrust on rudder effectiveness. Baseline configuration.

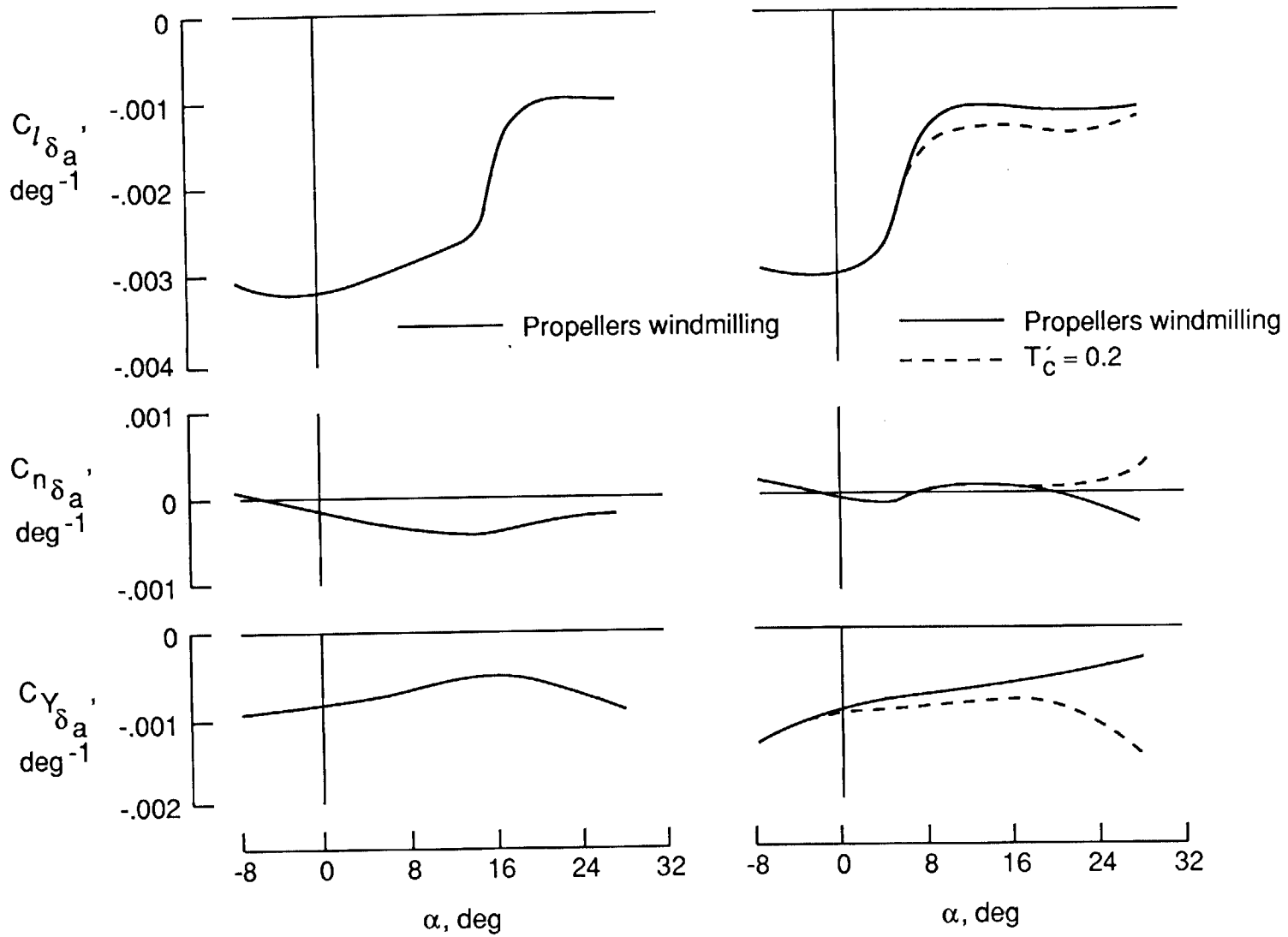

(a) Data from reference 3. $R_{\bar{c}} = 2.0 \times 10^6$.

(b) Data from present test. $R_{\bar{c}} = 0.5 \times 10^6$.

Figure 12. Effect of thrust on aileron effectiveness. Baseline configuration.

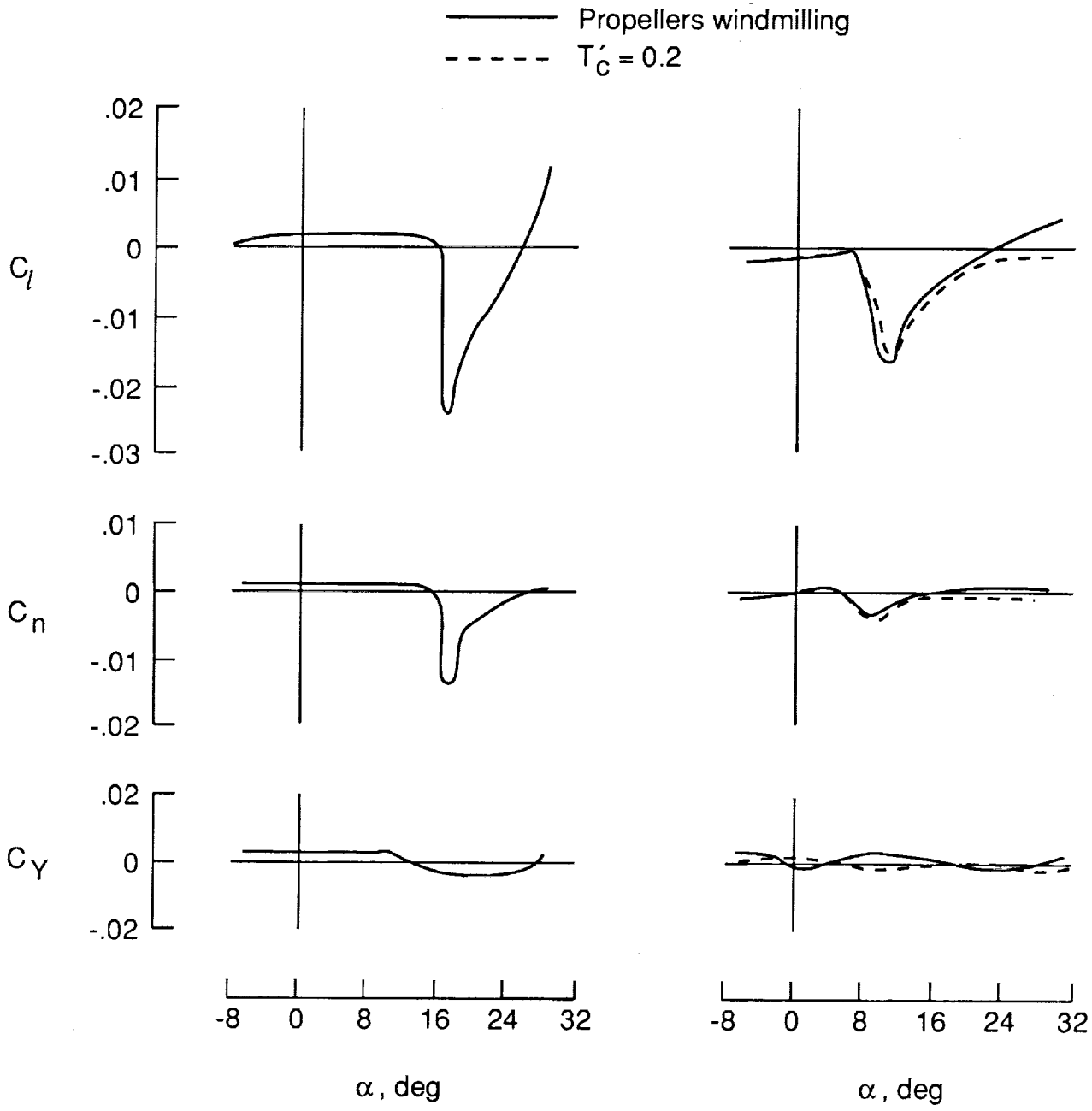

(a) Data from reference 3. $R_{\bar{c}} = 2.0 \times 10^6$.

(b) Data from present test. $R_{\bar{c}} = 0.5 \times 10^6$.

Figure 13. Variation of lateral-directional characteristics with angle of attack at $\beta = 0°$. Baseline configuration.

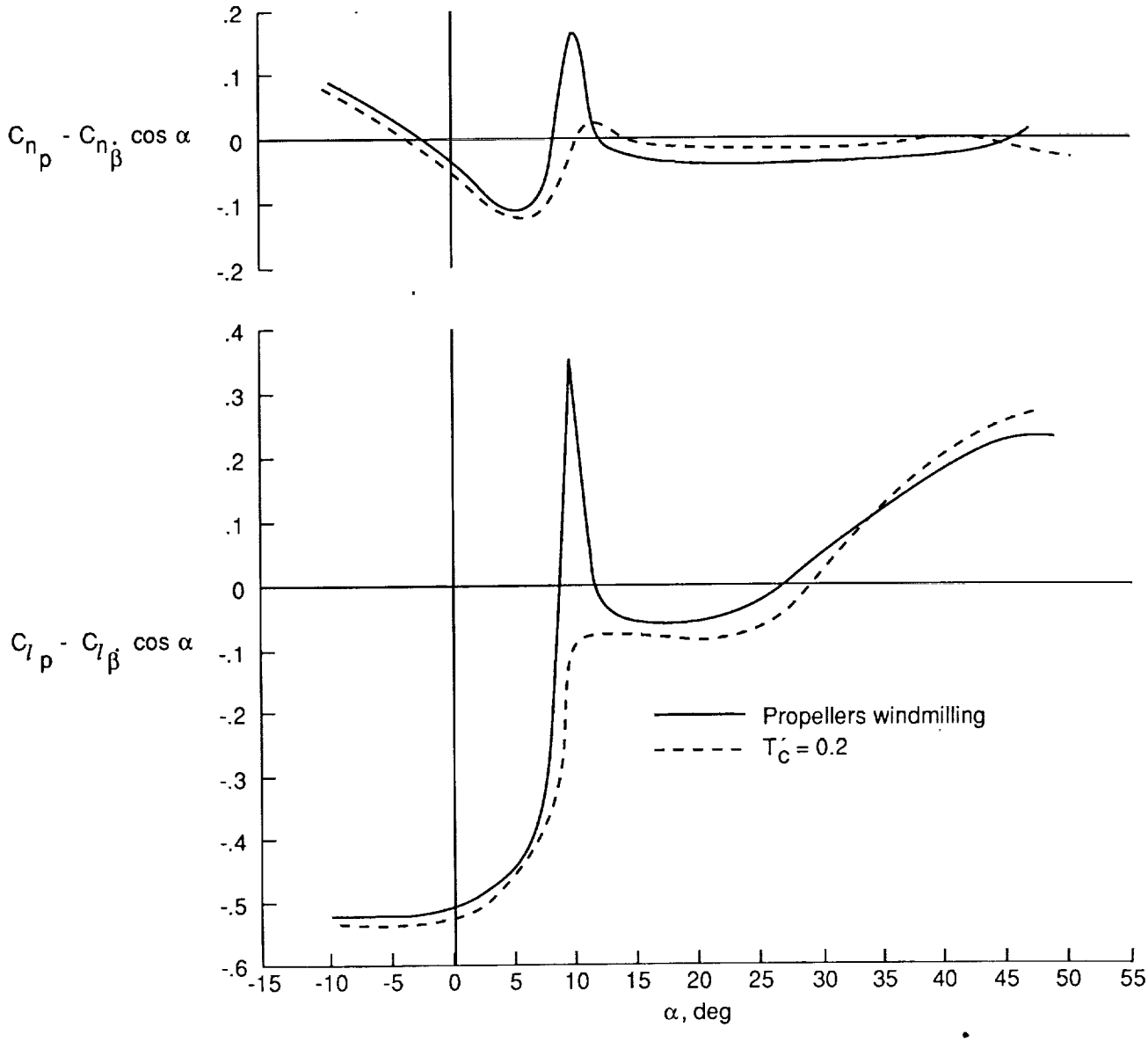

Figure 14. Effect of power on roll-damping characteristics. Baseline configuration.

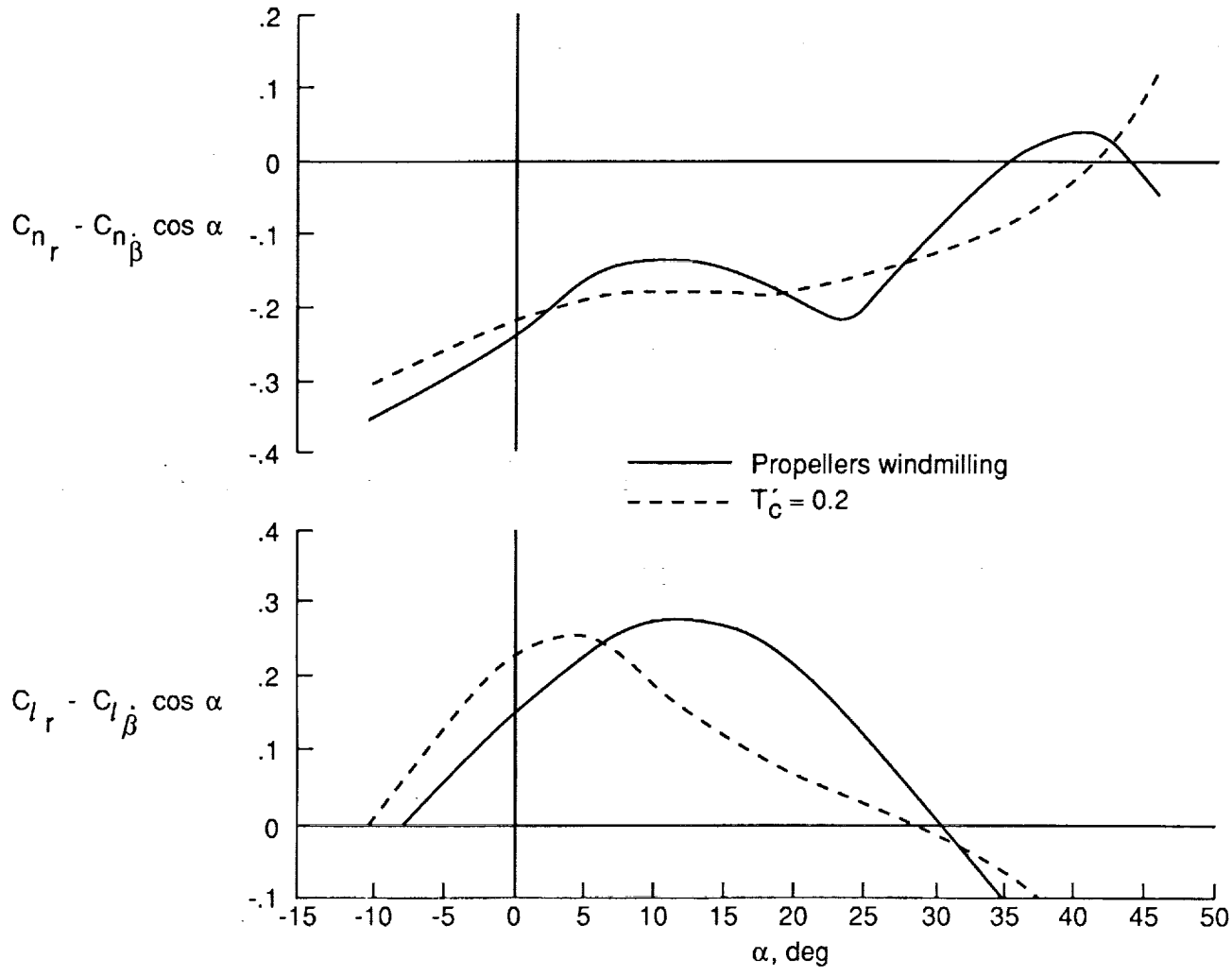

Figure 15. Effect of thrust on yaw-damping characteristics. Baseline configuration.

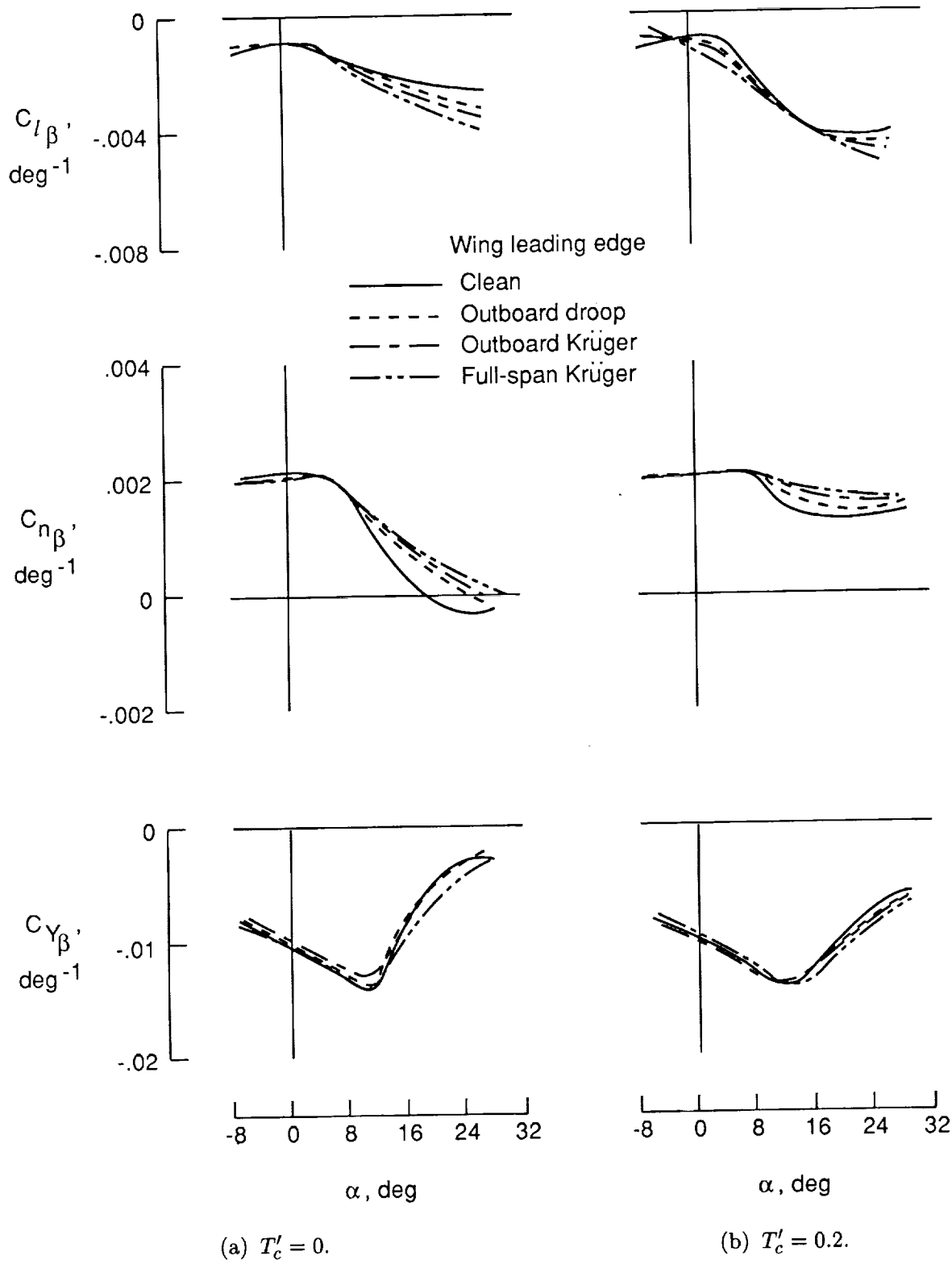

(a) $T_c' = 0.$

(b) $T_c' = 0.2.$

Figure 16. Effect of wing leading-edge devices on static lateral-directional stability characteristics.

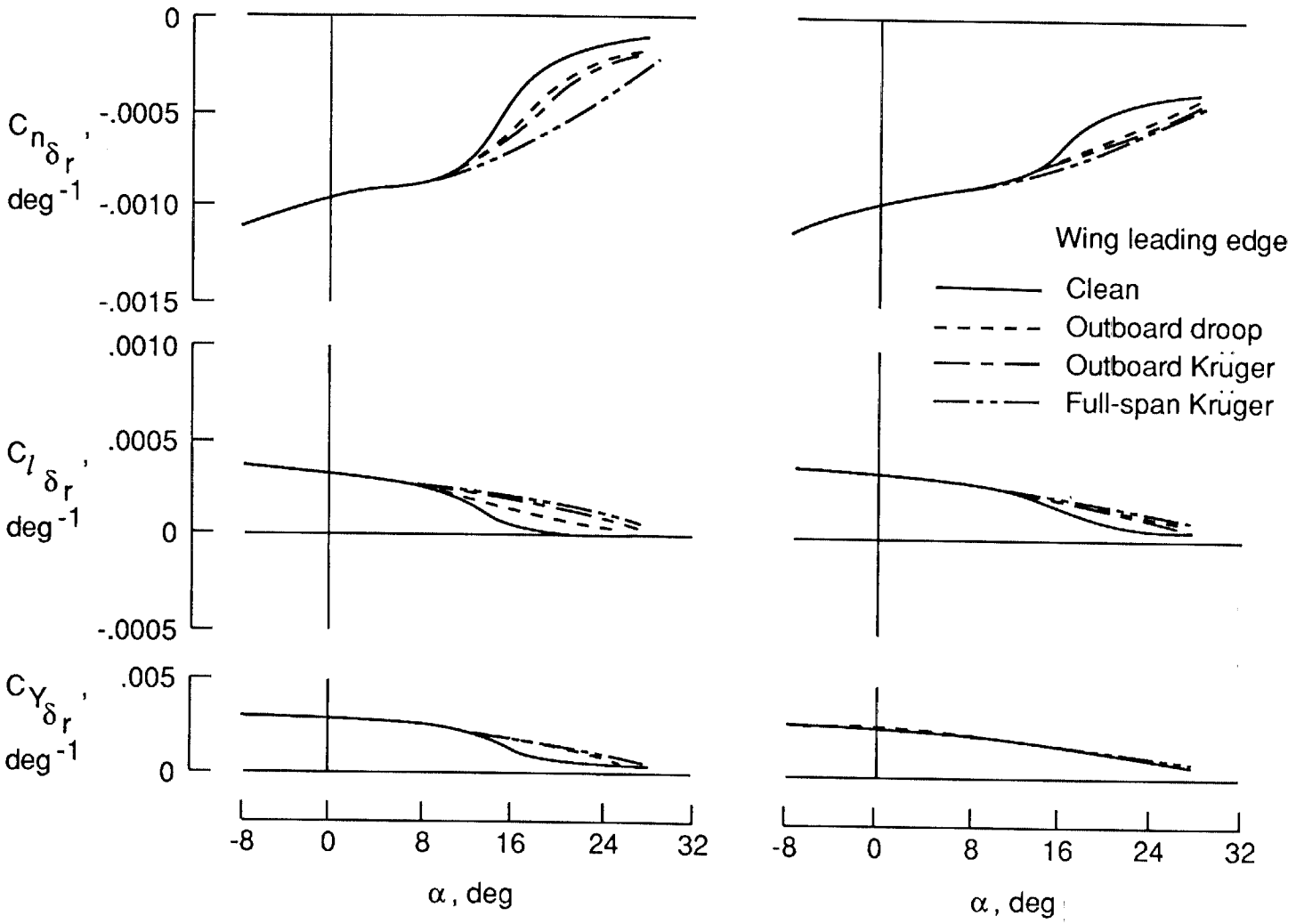

(a) $T_c' = 0.$

(b) $T_c' = 0.2.$

Figure 17. Effect of wing leading-edge devices on rudder effectiveness.

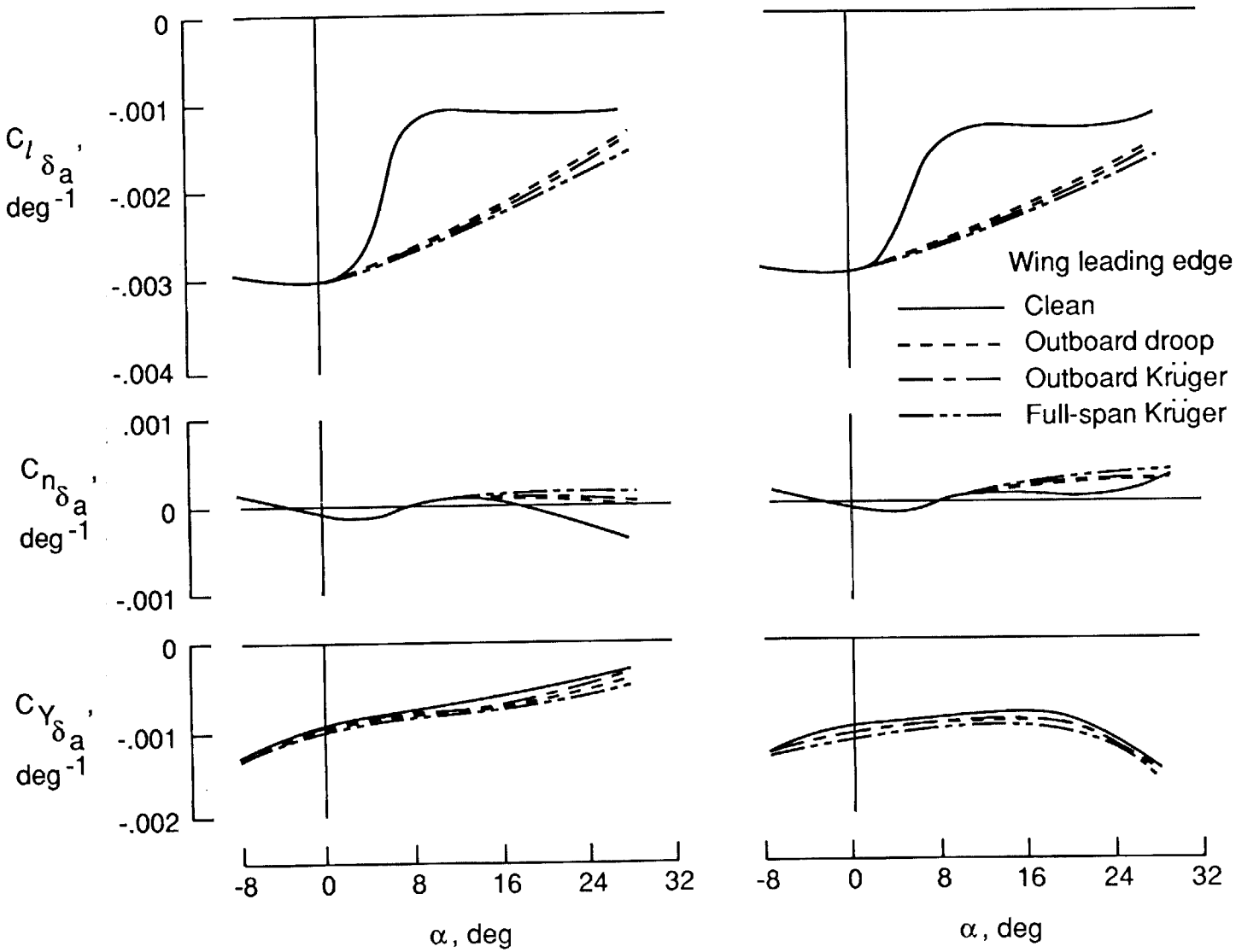

(a) $T_c' = 0$.

(b) $T_c' = 0.2$.

Figure 18. Effect of wing leading-edge devices on aileron effectiveness.

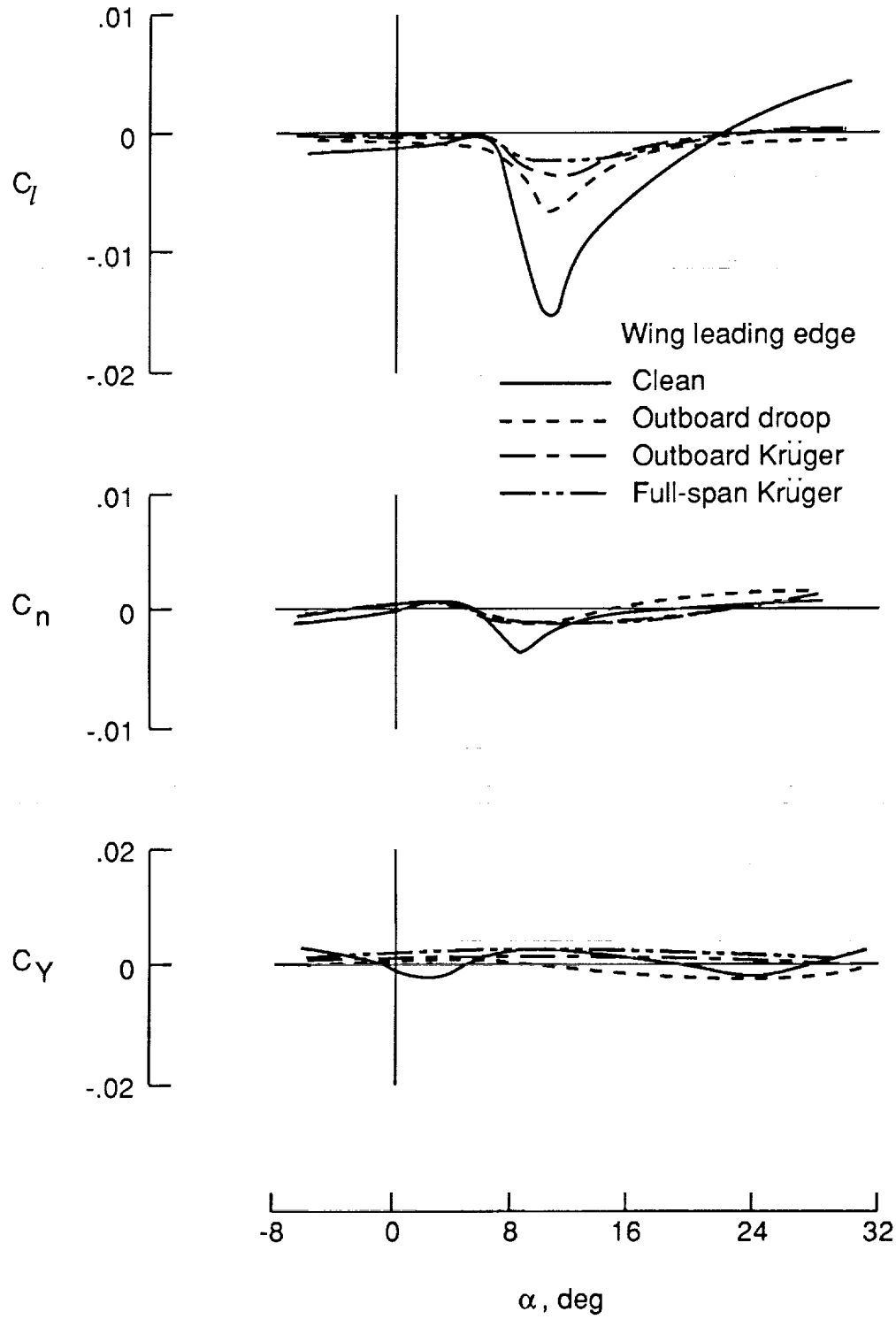

Figure 19. Effect of wing leading-edge devices on lateral-directional characteristics at $\beta = 0°$. $T_c' = 0$.

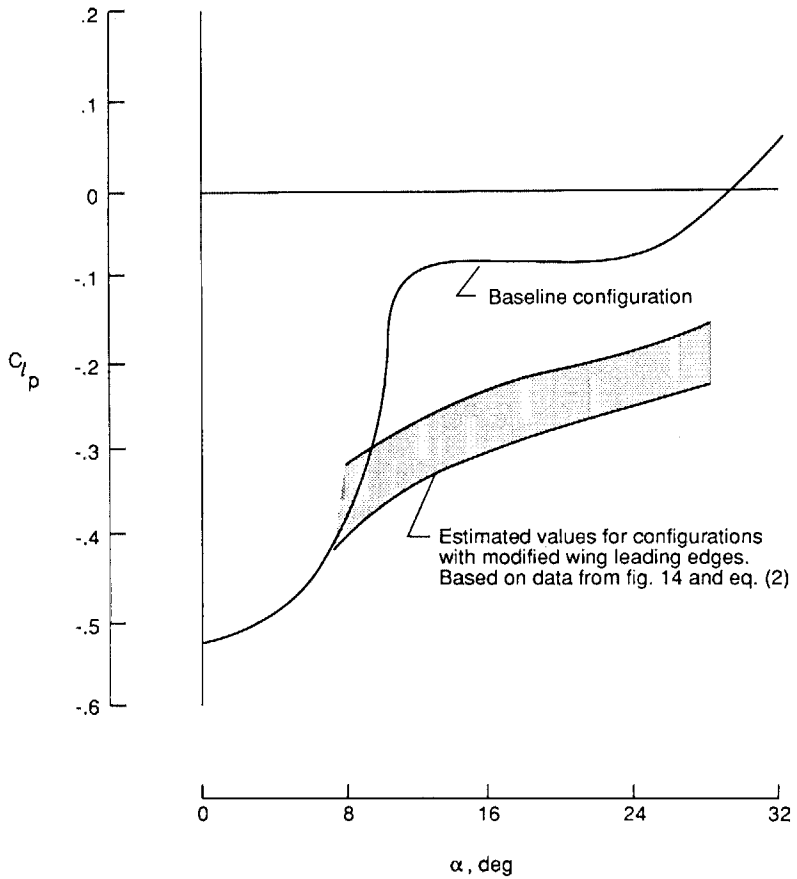

Figure 20. Effect of wing leading-edge devices on roll damping. $T_c' = 0.2$.

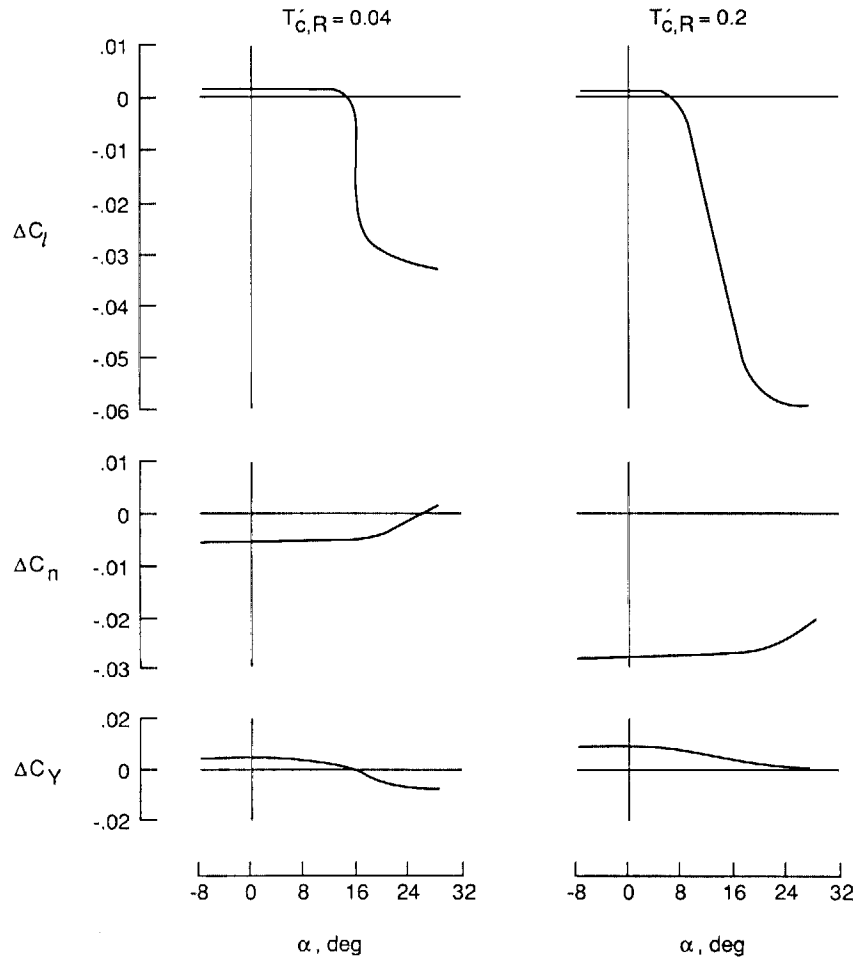

(a) Data from reference 3. $R_{\bar{c}} = 2.0 \times 10^6$.

(b) Data from present test. $R_{\bar{c}} = 0.5 \times 10^6$.

Figure 21. Engine-out characteristics with left engine inoperative. Baseline configuration.

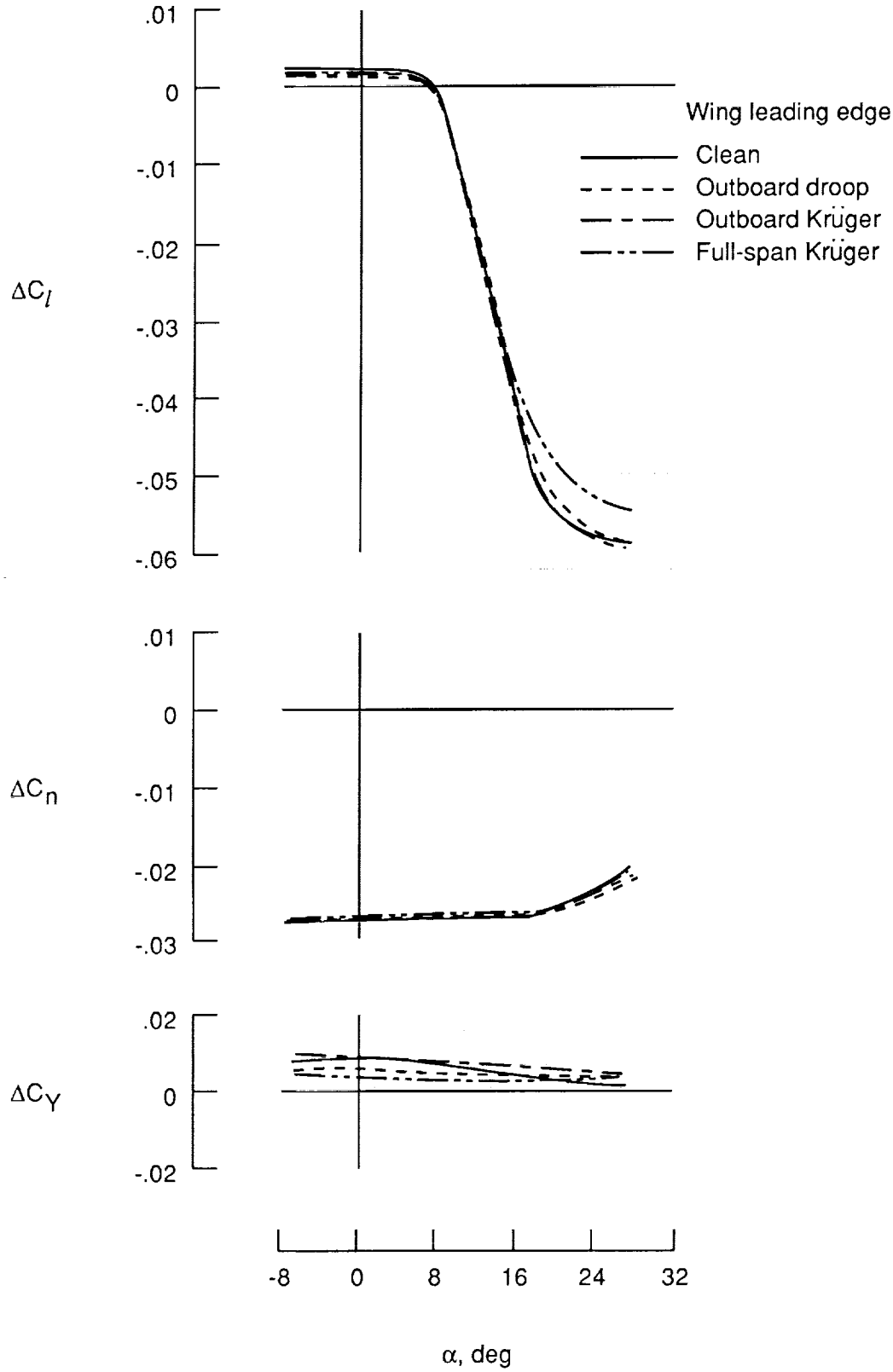

Figure 22. Effect of wing leading-edge devices on engine-out characteristics with left engine inoperative. $T'_{c,R} = 0.2$.

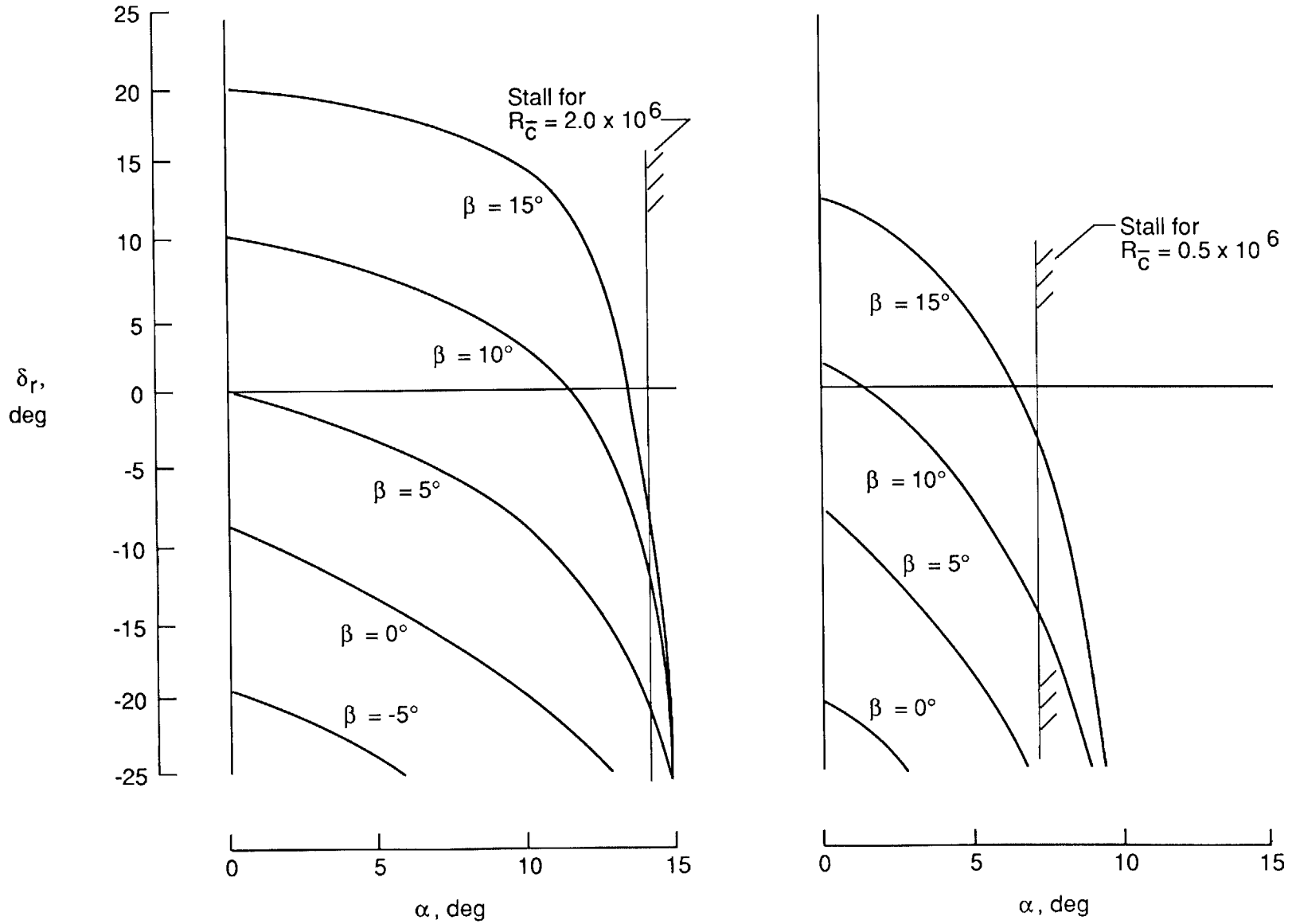

(a) Data from reference 3. $R_{\bar{c}} = 2.0 \times 10^6$.

(b) Data from present test. $R_{\bar{c}} = 0.5 \times 10^6$.

Figure 23. Rudder deflection required for left-engine-out yaw trim. Calculations based on equation (4); baseline configuration.

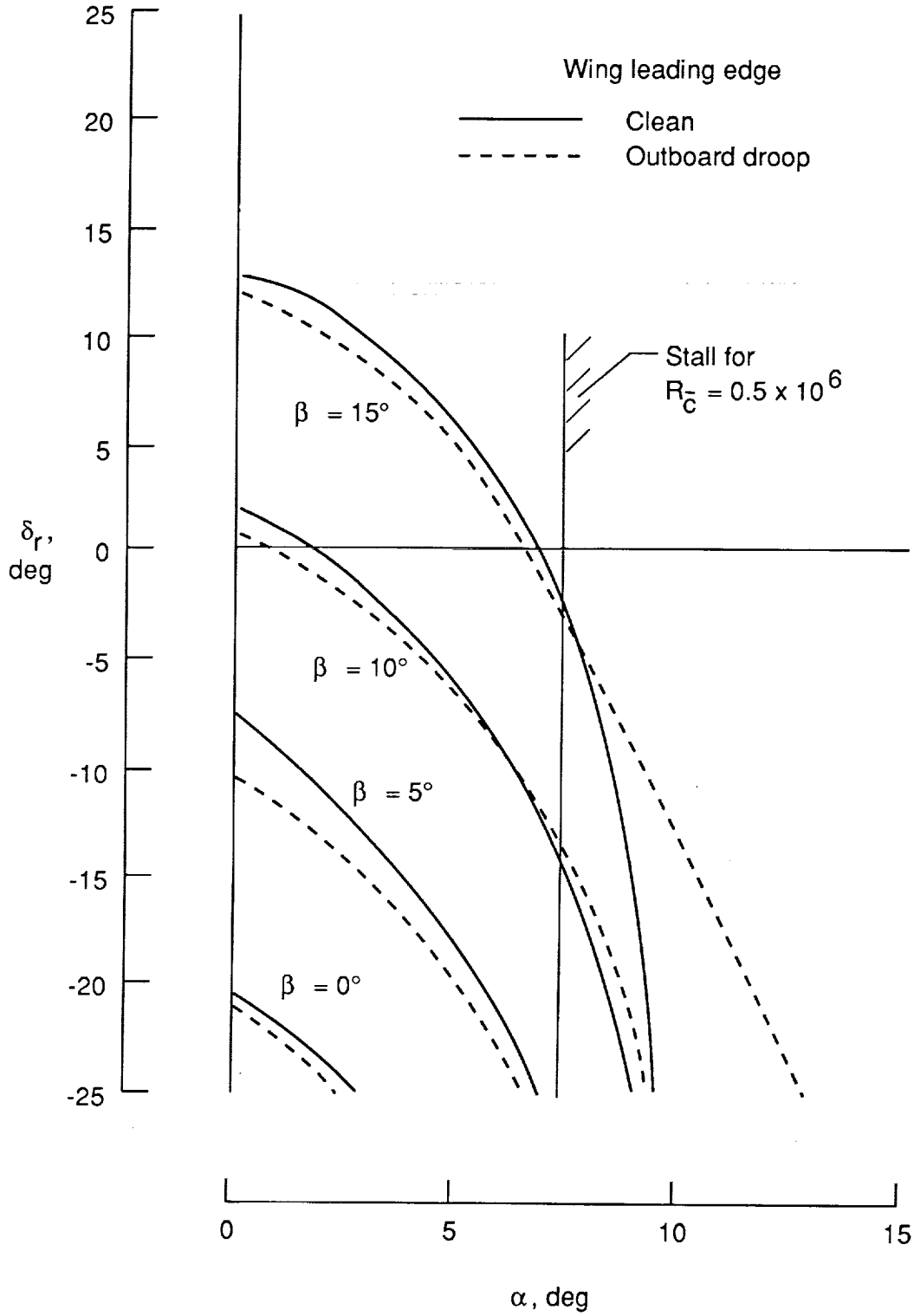

Figure 24. Effect of wing leading-edge device on rudder deflection required for yaw trim with left engine inoperative. Calculations based on equation (4).

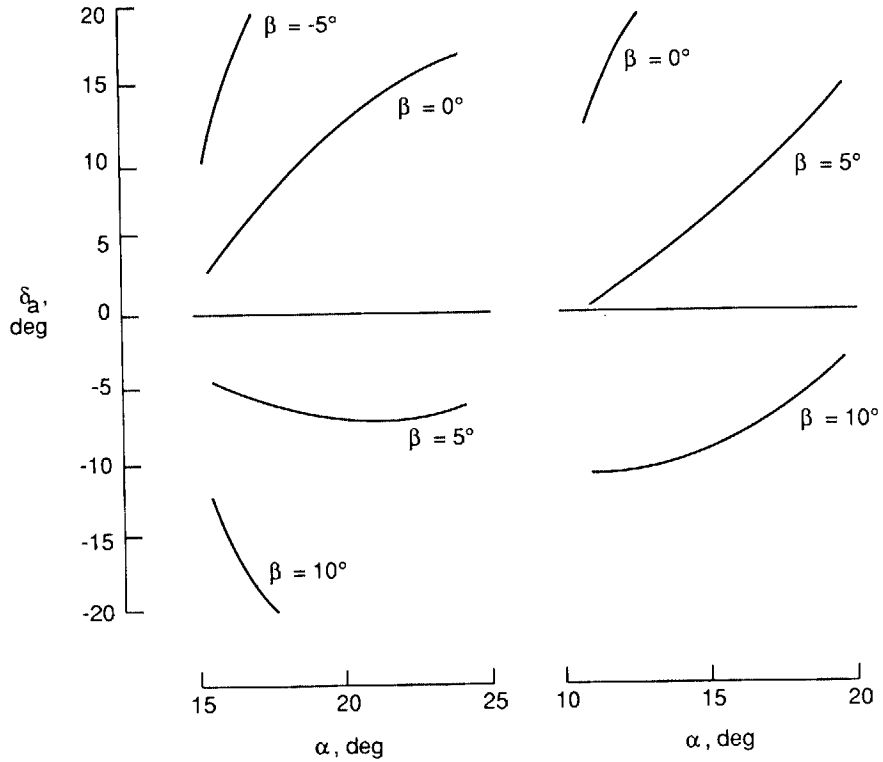

(a) Data from reference 3. $R_{\bar{c}} = 2.0 \times 10^6$.

(b) Data from present test. $R_{\bar{c}} = 0.5 \times 10^6$.

Figure 25. Aileron deflection required for left-engine-out roll trim. Calculations based on equation (7); baseline configuration.

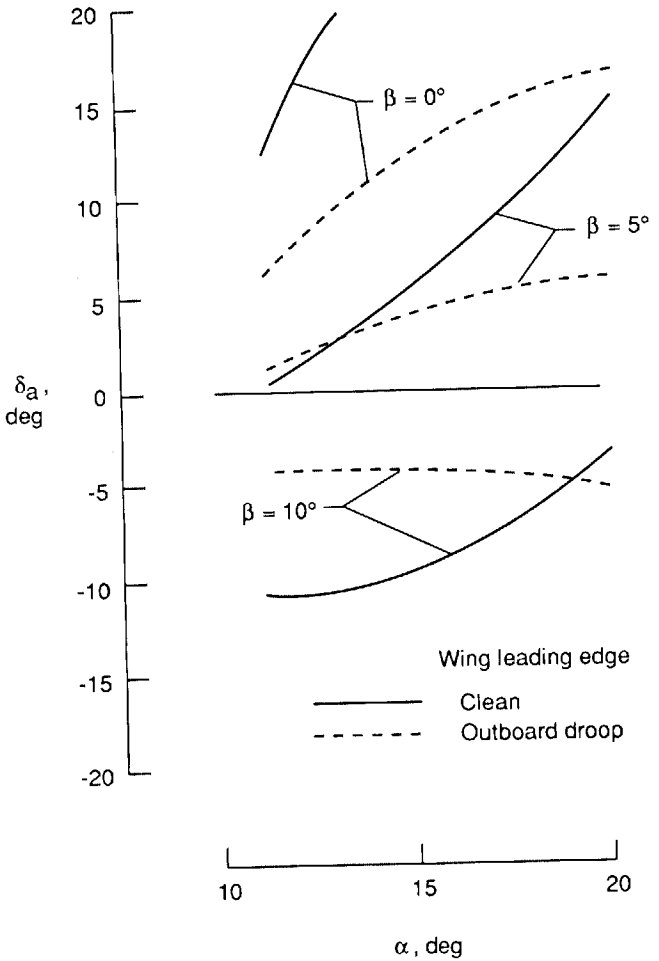

Figure 26. Effect of wing leading-edge device on aileron deflection required for left-engine-out roll trim. Calculations based on equation (7).

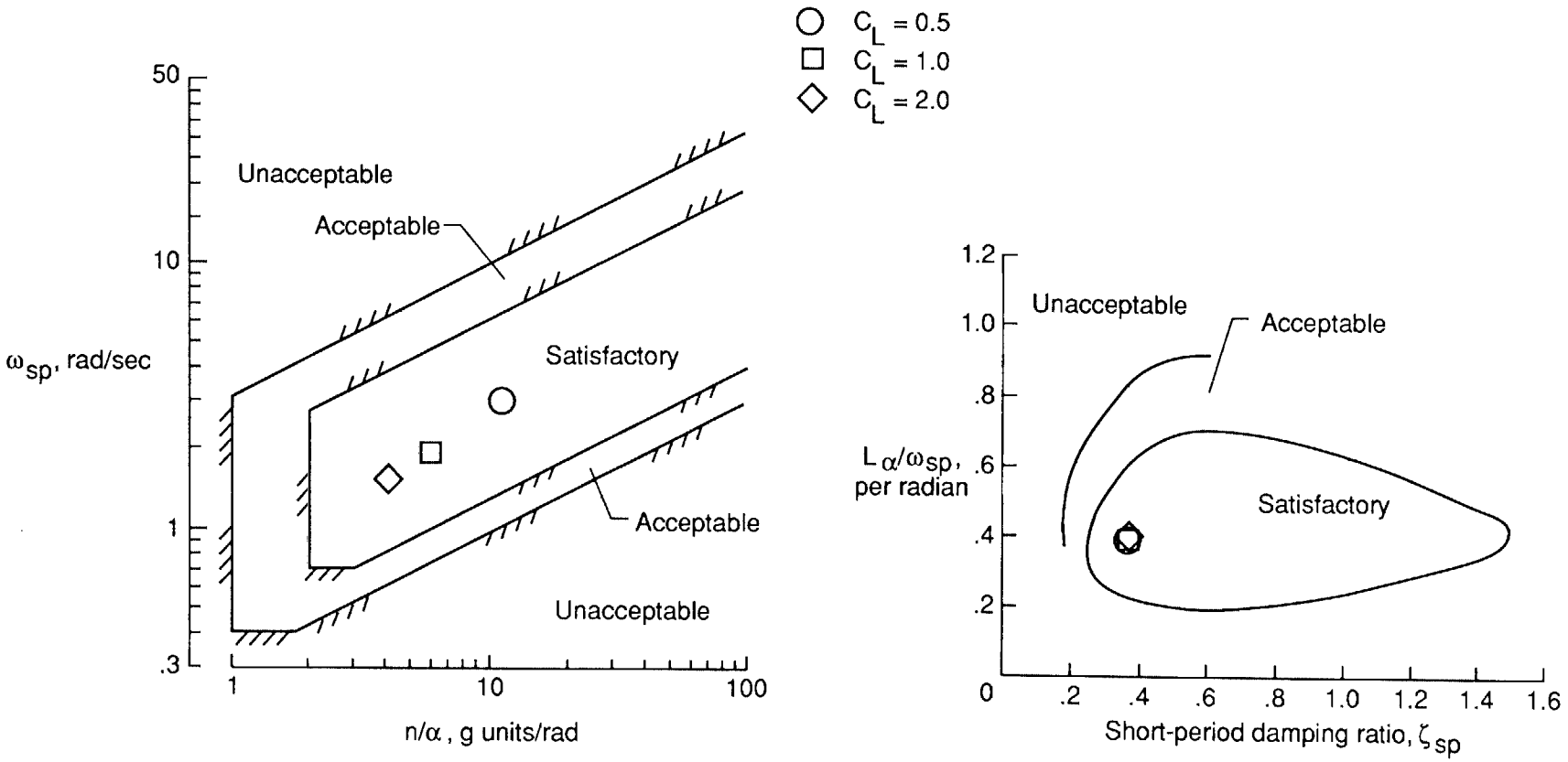

(a) Criterion from reference 13.

(b) Criterion from reference 14.

Figure 27. Longitudinal flying qualities criteria.

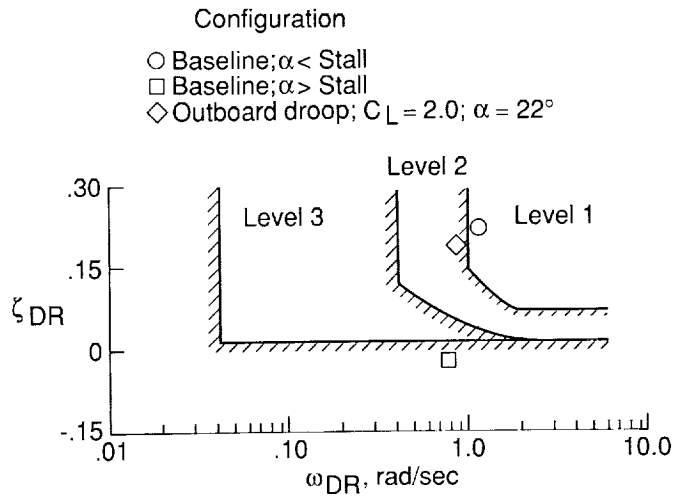

Figure 28. Dutch roll flying qualities. Requirements from reference 13.

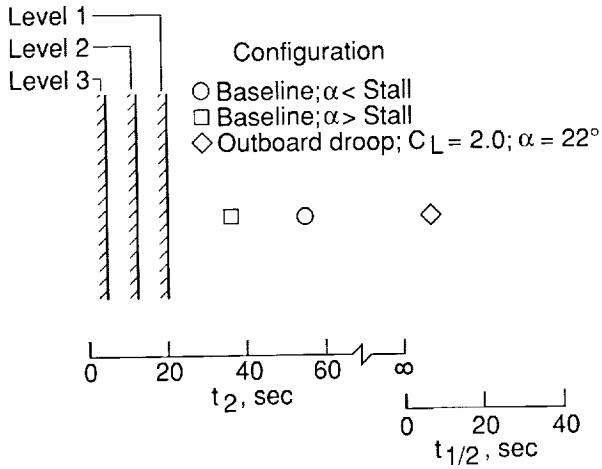

Figure 29. Spiral-mode flying qualities. Requirements from reference 13.

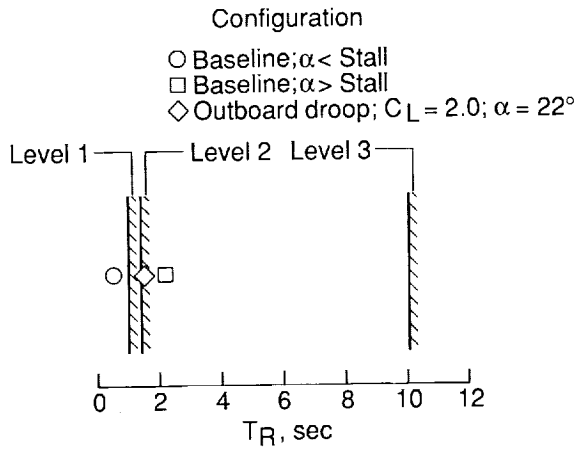

Figure 30. Roll-mode flying qualities. Requirements from reference 13.

NASA
National Aeronautics and Space Administration

Report Documentation Page

1. Report No.	2. Government Accession No.	3. Recipient's Catalog No.
NASA TP-2982		

4. Title and Subtitle	5. Report Date
Low-Speed Wind-Tunnel Investigation of the Flight Dynamic Characteristics of an Advanced Turboprop Business/Commuter Aircraft Configuration	April 1990
	6. Performing Organization Code
7. Author(s)	8. Performing Organization Report No.
Paul L. Coe, Jr., Steven G. Turner, and D. Bruce Owens	L-16664
9. Performing Organization Name and Address	10. Work Unit No.
NASA Langley Research Center Hampton, VA 23665-5225	505-62-41-07
	11. Contract or Grant No.
12. Sponsoring Agency Name and Address	13. Type of Report and Period Covered
National Aeronautics and Space Administration Washington, DC 20546-0001	Technical Paper
	14. Sponsoring Agency Code

15. Supplementary Notes

16. Abstract

An investigation was conducted to determine the low-speed flight dynamic behavior of a representative, advanced turboprop business/commuter aircraft concept. The investigation was conducted using model free-flight tests in the Langley 30- by 60-Foot Tunnel. In support of the free-flight tests, conventional static, dynamic, and free-to-roll oscillation tests were performed. Tests were intended to explore normal operating and poststall flight conditions and conditions simulating the loss of power in one engine.

17. Key Words (Suggested by Authors(s))	18. Distribution Statement
Flight dynamics Advanced turboprop aircraft Flying qualities	Unclassified—Unlimited Subject Category 08

19. Security Classif. (of this report)	20. Security Classif. (of this page)	21. No. of Pages	22. Price
Unclassified	Unclassified	48	A03

NASA FORM 1626 OCT 86

NASA-Langley, 1990

For sale by the National Technical Information Service, Springfield, Virginia 22161-2171